The Astrophysical Journal, 999:180 (17pp), 2026 March 10 https://doi.org/10.3847/1538-4357/ae40fd

ATOMS-QUARKS Survey: Inflow and Infall in Massive Protocluster G318.049+00.086 — Evidence of Competitive Accretion

Shivani Gupta[1,2,3], Tapas Baug[3], Archana Soam[1,2], Tie Liu[4,5], Fengwei Xu[6], Satyajeet Moharana[7,8], Guido Garay[9,10], Chang Won Lee[7,8], Siju Zhang[11], Ariful Hoque[3], Puja Porel[1,2], Lei Zhu[9], Dongting Yang[12], HongLi Liu[13], Wenyu Jiao[14,15], Xunchuan Liu[4], Alik Panja[1], Xiaofeng Mai[4], Yankun Zhang[4], and Shinyoung Kim[7]

[1] Indian Institute of Astrophysics, Koramangala II Block, Bangalore 560034, India; shivani.gupta@iiap.res.in
[2] Pondicherry University, R.V. Nagar, Kalapet, 605014, Puducherry, India
[3] S.N. Bose National Centre for Basic Sciences, Sector-III, Salt Lake, Kolkata 700106, India
[4] Shanghai Astronomical Observatory, Chinese Academy of Sciences, 80 Nandan Road, Shanghai 200030, People's Republic of China
[5] Key Laboratory for Research in Galaxies and Cosmology, Shanghai Astronomical Observatory, Chinese Academy of Sciences, 80 Nandan Road, Shanghai 200030, People's Republic of China
[6] Max Planck Institute for Astronomy, Königstuhl 17, 69117 Heidelberg, Germany
[7] Korea Astronomy and Space Science Institute, 776 Daedeokdae-ro, Yuseong-gu, Daejeon 34055, Republic of Korea
[8] University of Science and Technology, 217 Gajeong-ro, Yuseong-gu, Daejeon 34113, Republic of Korea
[9] Chinese Academy of Sciences South America Center for Astronomy, National Astronomical Observatories, CAS, Beijing 100101, People's Republic of China
[10] Departamento de Astronomía, Universidad de Chile, Las Condes, 7591245 Santiago, Chile
[11] Departamento de Astronomía, Universidad de Chile, Camino el Observatorio 1515, Las Condes, Santiago, Chile
[12] School of Physics and Astronomy, Yunnan University, Kunming 650091, People's Republic of China
[13] Department of Astronomy, Yunnan University, Kunming 650091, People's Republic of China
[14] Kavli Institute for Astronomy and Astrophysics, Peking University, Beijing 100871, People's Republic of China
[15] Department of Astronomy, School of Physics, Peking University, Beijing 100871, People's Republic of China
Received 2025 November 11; revised 2026 January 16; accepted 2026 February 1; published 2026 March 2

Abstract

We present a gas kinematic study of the massive protocluster G318.049+00.086. The protocluster is reported to contain 12 prestellar core candidates and four protostellar cores. Filamentary structures are identified using the 1.3 mm dust continuum map, with four of them converging into a dense central region, forming a hub-filament system. High velocity gradients (10–20 km s^{-1} pc^{-1}) derived from position–velocity analysis of $H^{13}CO^+$ emission along three of those filaments are suggestive of mass inflow onto the central hub. A mass inflow rate higher than 10^3 $M_\odot$ Myr^{-1} along the filaments indicates that the central hub is capable of forming massive star(s). Investigation of $H^{13}CO^+$ and CCH spectral profiles revealed the majority of the cores having the characteristic blue asymmetric line profiles, a typical signature of gravitational collapse. The remaining few cores showed red asymmetric profiles, indicative of gas expansion. Also, the derived mass infall rates for the protostellar cores in the hub region are significantly higher in comparison to those located along the filaments. The mass–radius relation of the cores revealed that the cores with red profiles reside in the massive star formation regime. However, the global velocity gradient along the filaments suggests that these particular cores are losing material to the hub. Our results support a competitive accretion scenario of massive star formation where gas is expected to be funnelled from less gravitationally dominant cores to the cores located at the gravitationally favorable position.

Unified Astronomy Thesaurus concepts: Protoclusters (1297); Interstellar medium (847); Interstellar filaments (842); Star forming regions (1565); Molecular clouds (1072); Radio astronomy (1338); Stellar kinematics (1608)

1. Introduction

Massive stars ($\geqslant$8 $M_\odot$) are crucial agents in galactic evolution owing to their strong radiative feedback and powerful stellar winds, followed by an energetic supernova explosion toward the end of their lives. Yet, the formation mechanism of massive stars is still not full understood. Over the past decades, several theoretical models have been proposed to explain the formation of high-mass stars, though none have been conclusively validated observationally, primarily because of their rarity, rapid evolution, and their formation in deeply embedded clustered environments (F. H. Shu et al. 1987; I. A. Bonnell et al. 2007; M. R. Krumholz & J. C. Tan 2007; J. C. Tan et al. 2014; F. Motte et al. 2018).

Two basic classes of theory are under active study for the formation of massive stars: (1) core accretion models or turbulent core model, and (2) clump-fed models, such as competitive accretion model, inertial-inflow model, and global hierarchical collapse (GHC) model.

The turbulent core model assumes a formation mechanism similar to that of their lower mass counterparts in that the formation of a massive star starts from the collapse of an isolated massive prestellar core, which is the gas reservoir for the final stellar mass (C. F. McKee & J. C. Tan 2003; M. R. Krumholz et al. 2007). It assumes that stars of all masses form via disk-mediated accretion from dense isolated prestellar cores, except that massive stars need to overcome additional support mechanisms like radiation pressure and ionization feedback. Prestellar cores having mass >16 $M_\odot$ within 0.01–0.1 pc of the radius are considered as key evidence for the turbulent core model (D. Yang et al. 2025a). Notably, only a handful of studies have found the existence of massive prestellar cores (~20–30 $M_\odot$) that can lead

to the formation of massive stars (see J. C. Tan et al. 2013; M. Valeille-Manet et al. 2025; D. Yang et al. 2025a, for example). This low detection rate implies a very short lifetime for high-mass prestellar cores (F. Motte et al. 2018). Factors, such as strong magnetic fields, high temperature, and concentrated initial density profiles, are found to effectively contribute to reducing fragmentation within the massive prestellar core and thus lead to the formation of more massive cores for high-mass star formation (A. Palau et al. 2021; P. Sanhueza et al. 2025; D. Yang et al. 2025b).

In contrast, the competitive accretion model is a theoretical framework proposed to explain how massive stars form within clustered environments (I. A. Bonnell et al. 1997, 2001; I. A. Bonnell & M. R. Bate 2006; C. F. McKee & E. C. Ostriker 2007; R. J. Smith et al. 2009). In this model, all stars—both low-mass and massive stars—form from a low-mass gravitationally bound prestellar core as a seed. These prestellar cores are embedded in a common massive clump or molecular cloud, where the bulk of the gas is not bound to individual cores but rather to the gravitational potential of the entire stellar cluster. It only accounts for mass accretion due to the gravity of the growing protostars (Bondi–Hoyle accretion), neglecting the preexisting inflow at the larger scales.

The other subtype of clump-fed model is the inertial-inflow model. According to this model, the prestellar cores that evolve into massive stars have a broad mass distribution but can accrete gas from parsec scales reservoir through large-scale converging flows, with the parsec-scale region around the prestellar core being turbulent and gravitationally unbound (P. Padoan et al. 2020). However, contrary observations have revealed most of the galactic parsec-scale massive clumps to be gravitationally bound irrespective of their evolutionary timescale (T. Liu et al. 2016; J. S. Urquhart et al. 2018).

The GHC model (J. Ballesteros-Paredes et al. 2011; E. Vázquez-Semadeni et al. 2017) advocates a picture of molecular clouds in a state of hierarchical and chaotic gravitational collapse (multiscale infall motions), in which local centers of collapse develop throughout the cloud while the cloud itself is also contracting (E. Vázquez-Semadeni et al. 2019). This model predicts anisotropic gravitational contraction with longitudinal flow along filaments at all scales. It has been supported through observational evidence as well as numerical simulations (see V. Camacho et al. 2020, and references therein).

All these "clump-fed" models assume that massive stars are born with low stellar masses but grow to much larger final stellar masses by accumulating mass from large-scale gas reservoirs beyond their natal dense cores. In these models, large-scale converging flows or global collapse of clumps are required to continuously feed mass into the dense cores.

Recent observations revealed that massive star-forming regions frequently show evidence of large-scale inflow along filaments spanning from 0.1 to several parsecs (H. Kirk et al. 2013; Q. Zhang et al. 2015). This challenges the notion of isolated massive turbulent cores and supports a picture where hubs and cores build up mass dynamically via filamentary accretion.

Protoclusters provide a valuable glimpse into the early stages of clustered star formation, as they contain both prestellar and protostellar cores embedded within filamentary structures. These systems offer a unique opportunity to study large-scale inflows and small-scale infall processes simultaneously, which are essential for understanding how gas is channeled from parsec scales down to individual cores (M. S. N. Kumar et al. 2020; D. Yang et al. 2023). In this paper, we studied the multiscale gas dynamics of a massive protocluster (G318.049+00.086), which has reported evidence of the presence of multiple filaments and several prestellar and protostellar cores to understand the underlying star formation mechanism.

1.1. Selected Region

The protocluster G318.049+00.086, also known as I14498-5856, is located at a distance of $2.90^{+0.52}_{-0.47}$ kpc (M. J. Reid et al. 2019) and has a local standard of rest velocity ($V_{\rm lsr}$) of $-49.82\,{\rm km\,s^{-1}}$ (Y.-H. Yue et al. 2021). The mass and dust temperature ($T_{\rm dust}$) of the protocluster are 1023.3 $M_\odot$ and 26.7 K, respectively (J. S. Urquhart et al. 2018). Using the CO(4–3) line, Y.-H. Yue et al. (2021) also reported that the global infall velocity and mass infall rate for this cluster are $V_{\rm in} = 3.77 \pm 0.07\ {\rm km\ s^{-1}}$ and $\dot{M}_{\rm in} = (1.56 \pm 0.03) \times 10^4\ M_\odot\ {\rm Myr^{-1}}$, respectively.

Recently, F. Xu et al. (2024a) identified 16 dense cores in the protocluster using the 870 μm dust continuum map observed using the Atacama Large Millimeter/submillimeter Array (ALMA; see their Figure 2(b)) and also derived several physical parameters (such as mass, radius, temperature, and surface density) of all the cores. Further, they also classified these cores as prestellar core candidates or protostellar cores based on their association with the bipolar outflows traced in the CO (3–2) line by T. Baug et al. (2020). In total, they reported the presence of four protostellar cores and 12 prestellar core candidates in this protocluster. We adopted these cores in our analyses. In this paper, we analyzed the filamentary structures traced by the 1.3 mm dust continuum and velocity distribution along their skeletons using $H^{13}CO^+$ (1–0), as well as infalling motions toward the embedded dense cores using $H^{13}CO^+$ (1–0) and CCH ($J = 3/2$–$1/2$) F(2–1) to look for the observational evidence for the massive star formation theory. Figure 1 represents the 3 mm (left panel) and 1.3 mm (right panel) dust continuum maps of the protocluster obtained from the ALMA Three-millimeter Observations of massive Star-forming regions (ATOMS) and Querying Underlying mechanisms of massive star formation with ALMA-Resolved gas Kinematics and Structures (QUARKS) surveys, respectively (see Section 2 for the surveys). The adopted protostellar cores and prestellar core candidates are represented as red and black ellipses, respectively.

Note that cores 15 and 16 are not present within the field of view of the 1.3 mm QUARKS data. Hence, we have not considered these cores in our subsequent analysis. Moreover, cores 1, 2, 3, and 4 are also excluded from further analysis. Core 1 is located significantly away from the main filamentary structure identified in the 1.3 mm QUARKS continuum map (Section 3.1), while cores 2, 3, and 4 appear to be tracing elongated filamentary material rather than distinct compact cores. This difference likely arises from the varying spatial filtering and sensitivity between the datasets, as the ALMA Survey of Star Formation and Evolution in Massive Protoclusters with Blue Profiles (ASSEMBLE) data include only the 12 m array, whereas the QUARKS data combine the 12 and 7 m arrays, enabling better recovery of extended emission.

The structure of the paper is as follows. In Section 2, we present the observations and data used in this study. Section 3 elaborates on the analysis and results obtained from the observed data. In Section 4, we discuss the overall gas dynamics and the star formation scenario in the region. Finally, we summarize our results in Section 5.

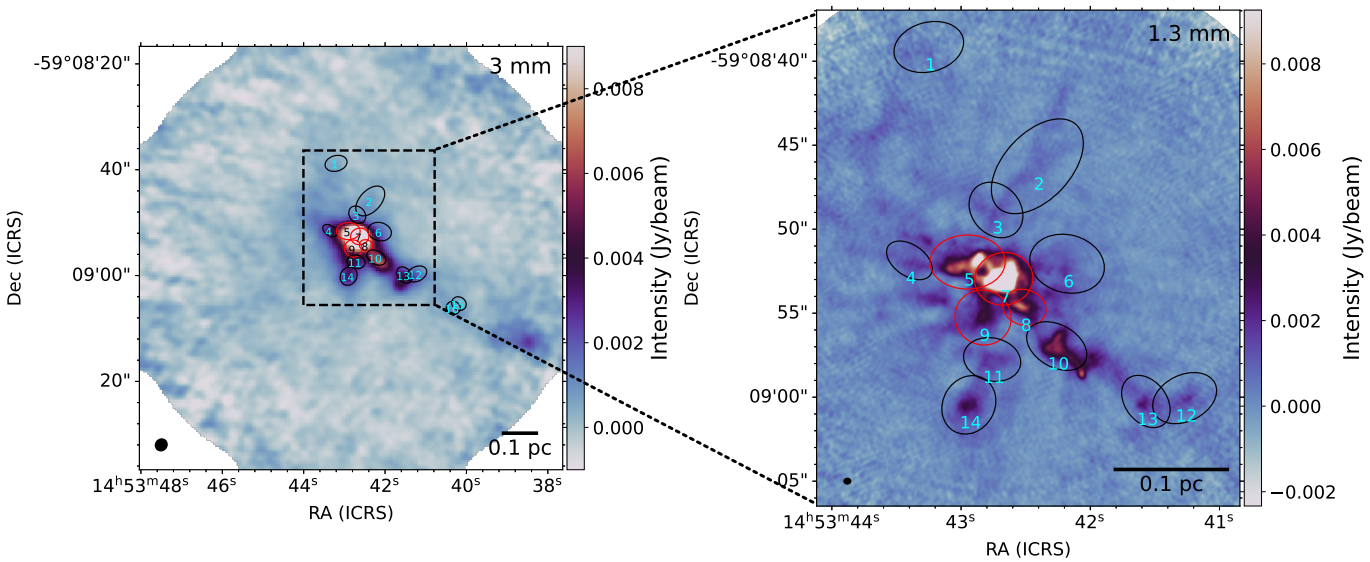

Figure 1. The continuum map of the protocluster at 3 mm (left panel) from the ATOMS survey and 1.3 mm (right panel) from the QUARKS survey. The overlaid ellipses denote the dense cores (red: protostellar cores, black: prestellar core candidates) identified at 870 μm by F. Xu et al. (2024a). The beam size and a scale bar are added at the bottom left and right corners of each panel.

2. Observations and Data Reduction

2.1. ATOMS Survey

ALMA data for the protocluster were obtained as part of the large survey ATOMS (Project ID: 2019.1.00685.S; PI: Tie Liu). Calibration of the 12 m array data and Atacama Compact Array (ACA) data was done separately using the Common Astronomy Software Applications (CASA) package version 5.6 (J. McMullin et al. 2007), and subsequently the visibility data were combined and reimaged to recover the extended emission. The maximum recoverable scale (MRS) of 12 m + ACA combine data reaches $\sim 87''$ (F.-W. Xu et al. 2023). Further details about the survey and data reduction can be found in T. Liu et al. (2020). All the images used in our analysis are primary beam corrected. The 3 mm (~99.93 GHz) dust continuum map has a beam size of $2\farcs34 \times 2\farcs16$ is constructed using data from line-free spectral channels. In this study, we utilized the $H^{13}CO^+$ (1–0), CCH F(2–1), and CS (2–1) transitions, with spectral resolutions of 0.422, 0.419, and 2.973 km s^{-1}, respectively. The velocity-integrated intensity maps of all the molecules observed in the ATOMS survey are shown in Figure A1 (Appendix A).

2.2. ASSEMBLE Survey

The G318.049+00.086 protocluster was also observed as part of the ASSEMBLE survey (Project ID: 2017.1.00545.S; PI: Tie Liu). The MRS of this data is $\sim 8\farcs45$ (F.-W. Xu et al. 2023). High-density tracers such as $H^{13}CN$ (4–3) and hot-core molecular lines like CH_3OH ($13_{1,12}$–$13_{0,13}$) were employed to determine the core systemic velocity, with a spectral resolution of 0.98 km s^{-1} (F.-W. Xu et al. 2023; F. Xu et al. 2024a).

2.3. QUARKS Survey

Furthermore, G318.049+00.086 was observed as part of the QUARKS survey, complementing the ATOMS survey with an improved angular resolution ($\sim 0\farcs3$). The corresponding 1.3 mm dust continuum map is prepared from the available line-free spectral channels (X. Liu et al. 2024). QUARKS also have ACA observations (F. Xu et al. (2024b), Quarks paper II). The combined data have an MRS of $\sim 8\farcs45$ (F. Xu et al. 2024b). The ACA observations help to cover the missing flux up to $30''$, which is important to the science goals.

Table 1 summarizes all the lines and continuum data used in this study, along with their observational parameters.

3. Results

In this section, we present the analyses and results of the observed data. Filaments were already identified in the region by using $H^{13}CO^+$ in a previous study by J.-W. Zhou et al. (2022). In the following section, we elaborate on retracing the filament using $H^{13}CO^+$ and also on the identification of the filaments by using the 1.3 mm dust continuum in the region.

3.1. Identification of Filaments

J.-W. Zhou et al. (2022), as part of the ATOMS survey, identified filamentary structures in this protocluster by applying the Python-based FilFinder algorithm (E. W. Koch & E. W. Rosolowsky 2015) on the moment 0 map of $H^{13}CO^+$ emission. In our analysis, the previously identified filamentary structures were well-reproduced with the same FilFinder algorithm. The identified filaments are shown in Figure 2(a). In addition to the main filament spine, FilFinder also identifies extended branches, shown in green, while the longest filament is highlighted in red (see Figure 2(a)).

We also employed the FilFinder algorithm on the 1.3 mm continuum map obtained in the QUARKS survey, as the continuum emission has good spatial resolution. The identified filaments are shown in Figure 2(b). The filaments were also labeled as F1, F2, F3, and F4. Positions of the cores identified by F. Xu et al. (2024a) are also marked in the figure. As can be seen in the figure, 12 out of the 14 identified cores are associated with these filaments.

In Figure 2(c), we overlaid the filamentary structures obtained from $H^{13}CO^+$ and 1.3 mm continuum emission to examine their spatial correlation. We note that the longest filaments obtained from both emissions strongly coincide with

Table 1
Main Molecular Lines Targeted in this Study

Species	Transition	Rest Frequency (GHz)	δv (km s^{-1})	Beam Size (arcsec)	rms (mJy beam^{-1})	Spatial Scale (pc^2)
ATOMS survey—ALMA Band 3 (12 m + ACA Combined)						
3 mm continuum	⋯	⋯	⋯	2.34 × 2.16	⋯	0.033 × 0.030
$H^{13}CN$	(1–0)	86.339918	0.424	2.34 × 2.16	11.3	0.033 × 0.030
$H^{13}CO^+$	(1–0)	86.754288	0.422	2.66 × 2.52	11.1	0.037 × 0.035
CCH	(1–0)	87.316898	0.419	2.63 × 2.50	11.3	0.037 × 0.035
CS	(2–1)	97.980953	2.973	2.36 × 2.18	5.0	0.033 × 0.031
ASSEMBLE survey—ALMA Band 6 (12 m only)						
CH_3OH	($13_{1,12}$–$13_{0,13}$)	342.729781	0.986	1.11 × 0.82	6.5	0.016 × 0.012
$H^{13}CN$	(4–3)	345.339760	0.980	1.08 × 0.80	6.3	0.015 × 0.011
QUARKS survey—ALMA Band 6 (12 m + ACA Combined)						
1.3 mm continuum	⋯	⋯	⋯	0.40 × 0.34	⋯	0.0056 × 0.0048

each other. This enables us to perform a comparative structural and dynamical analysis of the gas within the filaments.

3.2. Column Density Map

For a better understanding of the distribution of the gas, we constructed the column density map of the protocluster. To generate the map, we chose the $H^{13}CO^+$ line, and it was derived using the formula obtained under the assumption of local thermodynamic equilibrium (LTE) and the emission is optically thin (R. P. Garden et al. 1991),

$$N = \frac{3k_B}{8\pi^3 B\mu^2} \cdot \frac{\left(T_{ex} + \frac{hB}{3k_B}\right)}{(J+1)} \cdot \frac{\exp\left(\frac{hBJ(J+1)}{k_B T_{ex}}\right)}{1 - \exp\left(\frac{-h\nu}{k_B T_{ex}}\right)} \times \frac{1}{J(T_{ex}) - J(T_{bg})} \int T_{mb}\, dv, \quad (1)$$

where B and μ are the rotational constant and permanent dipole moment of the molecule, respectively, J is the rotational quantum number of the lower state in the observed transition, k_B is the Boltzmann constant, ν is the frequency and h is the Planck constant. $T_{bg} = 2.73$ K is the cosmic microwave background temperature, T_{mb} is the main beam brightness temperature, and T_{ex} is the excitation temperature. $J(T) = T_0/(e^{T_0/T} - 1)$ represents the source function, where $T_0 = h\nu/k_B$. For this $H^{13}CO^+$ (1–0) transition, we used $J = 0$, $\mu = 3.89$ D, and $B = 43.377302$ GHz (P. Botschwina et al. 1993; Y. Yamaguchi et al. 1994; V. Lattanzi et al. 2007; P. Sanhueza et al. 2012). With all these values, Equation (1) is simplified to

$$N(H^{13}CO^+) = 2.43 \times 10^{11} \cdot (T_{ex} + 0.69) \cdot \frac{1}{1 - \exp\left(\frac{-4.16}{T_{ex}}\right)} \times \left(\frac{4.16}{\exp\left(\frac{4.16}{T_{ex}}\right) - 1} - 1.16\right)^{-1} \int T_{mb}\, dv. \quad (2)$$

Under the assumption of LTE, all levels are populated according to the same excitation temperature (T_{ex}). In this calculation, we assume that T_{ex} is equal to the dust temperature of the clump (T_{dust}). $\int T_{mb}\, dv$ is the integrated intensity of the $H^{13}CO^+$ emission. For the construction of the column density map ($N(H^{13}CO^+)$), we considered only the pixels with integrated intensity $>5\sigma$ in the moment 0 map. The remaining pixels were masked out from the final map.

Conversion of the $N(H^{13}CO^+)$ column density map into hydrogen column density ($N(H_2)$) requires the $[H^{13}CO^+/H_2]$ abundance ratio. However, we found that the corresponding abundance varies from 10^{-10} to 10^{-12} depending on various physical conditions (e.g., G. A. Blake et al. 1987; M. A. Frerking et al. 1987; S. García-Burillo et al. 2000; T. Handa et al. 2006; M. Rodríguez-Baras et al. 2021; S. Zhang et al. 2024, and references therein). Thus, we derived the $N(H_2)$ from $N(H^{13}CO^+)$ using the mean of the reported abundance ratio of 10^{-11}. The final column density map of the region is presented in Figure 3. Note that the $N(H_2)$ ranges between 0.5 and 4.0) $\times 10^{24}$ cm^{-2}, with the highest being at the hub region.

The derived $N(H_2)$ value represents a lower limit to the true column density, as the assumption of the line to be optically thin is not always valid, specifically in the dense region (i.e., dense cores, discussed in later sections).

If we consider $H^{13}CO^+$ has a moderate opacity ($\tau \sim 0.5$–1.5), the optically thin assumption would underestimate the column density by a factor of $\tau/(1 - e^{-\tau})$, corresponding to an increase of approximately ∼27%–93% relative to the optically thin estimation. This translates directly into a similar increase in the derived filament mass. Further, we assumed a constant dust temperature (T_{dust}) across the region. A plausible uncertainty of ±10 K to our adopted value introduces an uncertainty of approximately 33% to 36% in the derived $N(H_2)$. Specifically, increasing the temperature by 10 K results in a ∼33% increase in the column density (and mass), while decreasing the temperature by 10 K leads to a ∼36% decrease. Finally, the conversion from $N(H^{13}CO^+)$ to $N(H_2)$ depends critically on the assumed abundance ratio. While we adopted a representative value of $[H^{13}CO^+/H_2] = 10^{-11}$, reported values span a wide range from 10^{-10} to 10^{-12}. Adopting these extreme values would decrease or increase the inferred column density by an order of magnitude, respectively, implying that the total mass estimates could vary by up to a factor of 10.

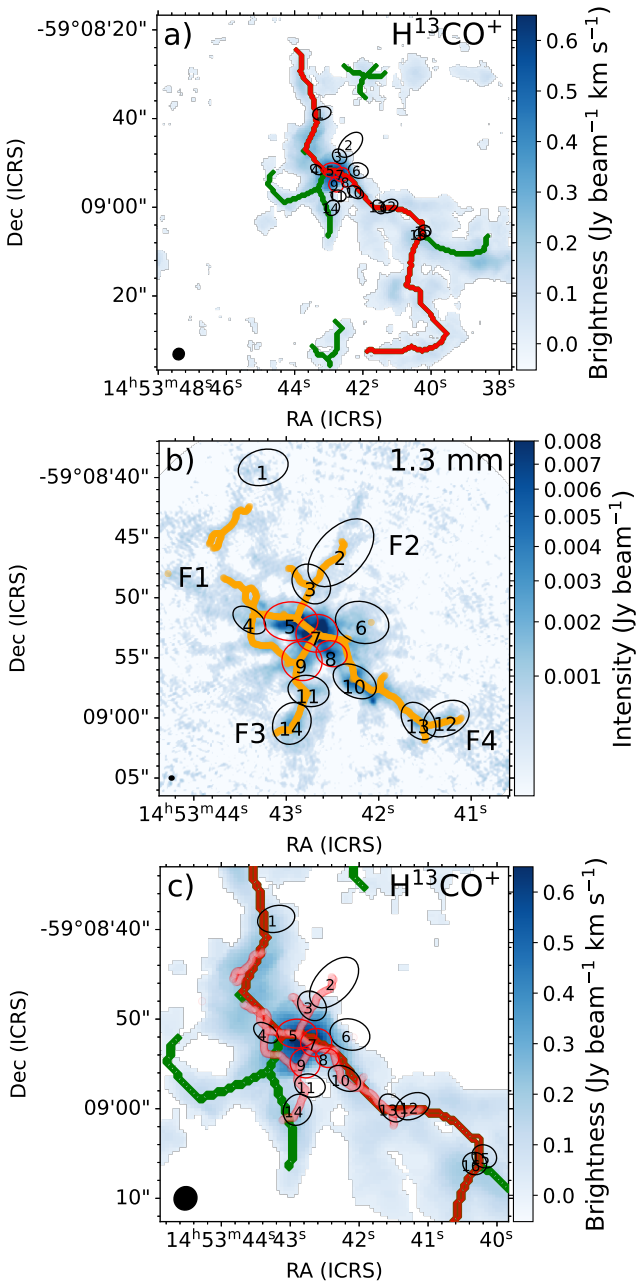

Figure 2. (a) The identified $H^{13}CO^+$ filaments overlaid on the moment 0 map of $H^{13}CO^+$ above the 5σ level. The red colored filament marks the longest filament, and the green shows other filaments present in the region. (b) Displays the filaments (orange lines) identified in the 1.3 mm continuum emission overlaid on the 1.3 mm dust continuum map of the protocluster. The primary filaments are also labeled as F1, F2, F3, and F4. (c) Overlay of $H^{13}CO^+$ and 1.3 mm filaments on $H^{13}CO^+$ moment 0. In all the panels, the identified cores by F. Xu et al. (2024a) are shown and labeled.

3.3. Dynamical Properties of Filaments

Figure 4 displays the moment 1 map (intensity-weighted velocity map) of $H^{13}CO^+$, overlaid with the filamentary structure from the 1.3 mm continuum, providing insight into the underlying velocity distribution. It has been reported in previous studies that the filaments play an important role in transporting gas and aiding in star formation. To assess such a possibility, we examined the position–velocity (PV) diagram of the filaments (S. Kim et al. 2022). The PV diagrams of the filaments were constructed by determining the centroid

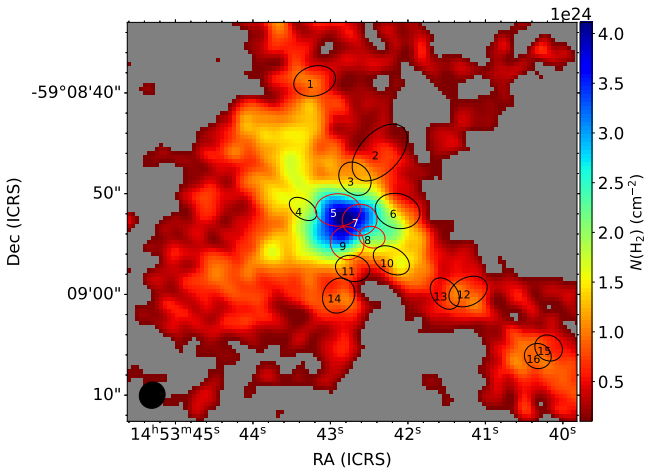

Figure 3. $N(H_2)$ column density map of the observed region derived using the $H^{13}CO^+$ line emission above the 3σ level. Positions of the cores identified by F. Xu et al. (2024a) are also marked in the figure.

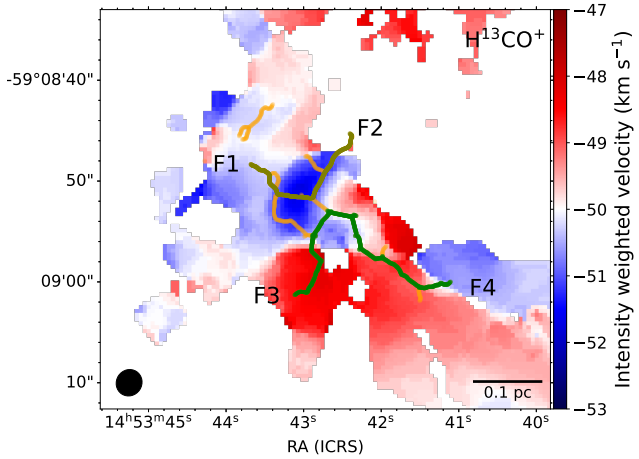

Figure 4. Filaments identified in the 1.3 mm continuum emission overlaid on the moment 1 map of $H^{13}CO^+$ (1–0). The olive and green colors mark the primary filament paths (i.e., F1-F2 and F3-F4, respectively) used to derive the PV diagrams.

velocity along each of these filament skeletons. Note that the four filaments labeled as F1, F2, F3, and F4 converge toward the central hub region. For convenience, we combined them in two groups, i.e., F1-F2 and F3-F4, for the construction of the PV diagrams and also to study the kinematics of the inflowing gas (see olive skeleton for F1-F2 and green skeleton for F3-F4 in Figure 4). The corresponding PV diagrams are presented in Figure 5. The starting point for both the PV diagrams was defined at the eastern end of filaments F1 and F3, respectively. It can be seen in both the PV diagrams that a global minimum is present toward the location of the hub, suggesting an inflow of gas along the filaments toward the hub. This inflow may facilitate conditions conducive to the formation of massive stars.

For estimation of the velocity gradients, we performed least-squares fits to different parts of the PV diagrams signifying the filaments (see Figure 5). The slopes of these fits represent the mean velocity gradients. The estimated velocity gradients along filaments F1, F3, and F4 are 22.5, 22.1, and 10.9 km s^{-1} pc^{-1}, respectively. The uncertainties for these gradients are obtained from the error associated with the least-squares fit (listed in Table 2). Note that we were unable to determine a

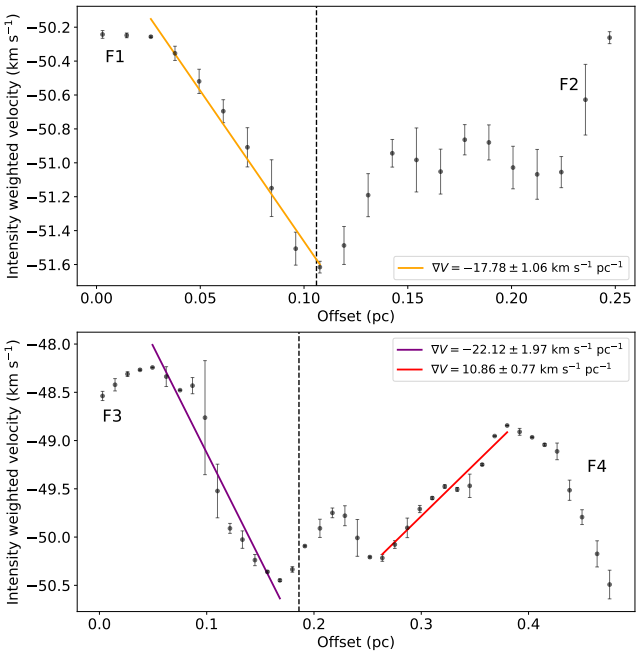

Figure 5. The upper panel shows the PV diagram along the filament path F1 and F2, and the lower panel shows the PV along F3 and F4. The PV diagrams are uniformly sampled along the filament skeletons with a step size of 0.016 pc, corresponding to half of the synthesized beam size at the source distance. The velocity error bars represent the standard deviation of the velocities within each sampled bin along the offset. The vertical-dashed line in each panel marks the position of the hub. The orange, purple, and red lines indicate the least-squares fit to the F1, F3, and F4 segments of the PV diagrams in both panels, respectively.

consistent velocity gradient along the filament F2 due to significant velocity fluctuations along this filament. J.-W. Zhou et al. (2022) also found velocity gradients using the $H^{13}CO^+$ along the largest path in the hub region, following the filamentary structure from F1 to F4.

Such high velocity gradients within very short distances (∼0.1–0.2 pc) indicate the dominance of gravity on inflow and accumulation of gas in dense cores or hub regions. In fact, J.-W. Zhou et al. (2022) noted that in other protoclusters in the ATOMS sample, the velocity gradients also increase drastically within shorter separations (∼10–40 km s^{-1} pc^{-1}) compared to those derived for larger separations (∼1 km s^{-1} pc^{-1} at 1.5 pc).

3.4. Mass Inflow Rate along the Filaments

For the estimation of the mass flow along the filaments, we first derived the mass of the filament segments that show the velocity gradients. The filament mass was estimated from the H_2 column density map. The calculated mass ($M_{\rm fil}$) and line mass ($m_{\rm fil}$) of the filaments are listed in Table 2. The uncertainty in $M_{\rm fil}$ is derived by adopting the uncertainty in distance to the protocluster (0.5 kpc) and the standard deviation in H_2 column density within the filament segment. The estimated filament masses are typical for galactic filaments of the order of 100 $M_\odot$. However, the estimated line mass of the filaments is found to be 992–1746 $M_\odot$ pc^{-1}, which is typical for giant filaments (see A. Hacar et al. 2023, for details). Such a high concentration of gas in these filaments is possibly due to their association with the massive protocluster.

To quantify the mass flow along the filaments, we followed a similar methodology described in H. Kirk et al. (2013). Assuming a simple cylindrical model, the equation for mass inflow rate of the axial flow motion can be written as

$$\dot{M}_{\parallel} = \frac{\nabla V_{\parallel} M_{\rm fil}}{\tan\alpha}, \quad (3)$$

where $\nabla V_{\parallel}$ is the velocity gradient measured along the filament, $M_{\rm fil}$ is the mass of the filament segment, and α is the angle between the axis of the cylinder and the plane of the sky. The mass inflow rates along the filaments F1, F3, and F4 were computed using the estimated filament masses and the velocity gradients (see Table 2), assuming an inclination angle (α) of 45°, and are found to be in the order of 10^3 $M_\odot$ Myr^{-1} (see also Table 2 for the exact values). Two extreme cases for α, i.e., 0° and 90°, signify the nonexistence of the observed velocity gradients along filaments and the nonexistence of the filaments, respectively. However, such possibilities can be excluded by the fact that filamentary structures do exist, and the velocity variation along them is also significantly measurable. We thus assume $\tan\alpha = 1$ in our calculation, and the estimated velocity gradients and mass inflow rates are expected to be uncertain by a factor of 2 when the α changes between 30° and 60° (M. R. A. Wells et al. 2025).

3.5. Gas Infall Rates in Cores

In the previous section, we noted the inflow of gas along the filaments. It is now important to examine the gas dynamics of the cores present in this protocluster. For the investigation of the potential collapse motions within the prestellar and protostellar cores, we analyze the spectrum of an optically thick tracer. The spectrum of such a tracer is often useful to identify the characteristic self-absorption features with asymmetric double-peaked line profiles. A stronger blue peak in the double-peaked profile compared to the red one is commonly referred to as the blue profile and is typically considered the signature of infalling gas. On the contrary, a double-peaked profile with a stronger red peak, known as the red profile, signifies the expanding gas. Occasionally, in the case of prestellar cores, red and blue profiles may signify infall and expansion motions, respectively (C. H. De Vries et al. 2002). Such a profile is generally expected when inversion of the temperature gradient occurs from the core to the envelope due to the presence of an external heating source (C. H. De Vries et al. 2002), but this is not the case here.

In general, tracers like HCO^+ (1–0) or CS (2–1) are best suited for this purpose. However, in our protocluster, the HCO^+ line is significantly contaminated by outflow activities from the embedded protostars, while the CS line has a coarse spectral resolution of about 3 km s^{-1} that can significantly distort these characteristic features.

Note that J.-W. Zhou et al. (2022) and S. Zhang et al. (2023) have reported asymmetric and double-peaked profiles in $H^{13}CO^+$ toward the densest regions in several protoclusters of the ATOMS survey. Interestingly, we also found asymmetric blue $H^{13}CO^+$ profiles for most of the cores, with the $V_{\rm lsr}$ of the protocluster lying close to the dip between the blue and red parts, indicating the self-absorption feature, deviating from its commonly assumed optically thin nature in dense cores. To further confirm this, we use optically thin tracers: CH_3OH

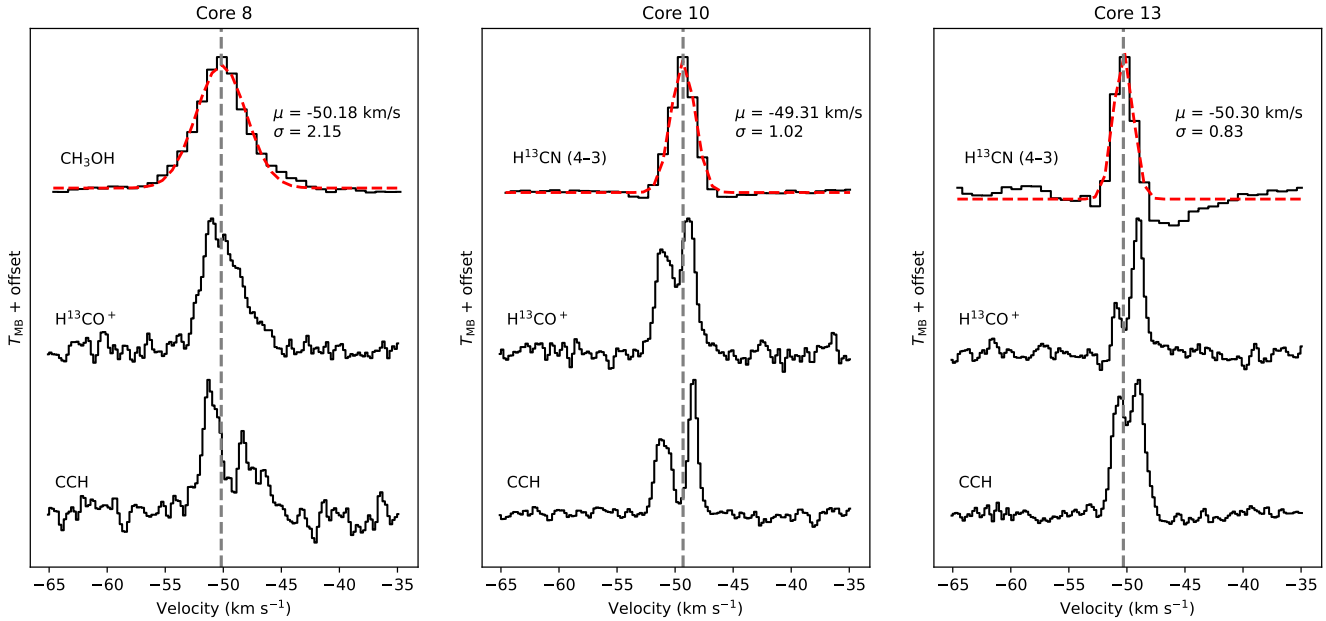

Figure 6. Average spectra of $H^{13}CO^+$, CCH, and CH_3OH ($13_{1,12}$–$13_{0,13}$)for core 8 and $H^{13}CN$ (4–3) for cores 10 and 13. The spectra of CH_3OH ($13_{1,12}$–$13_{0,13}$) and $H^{13}CN$ (4–3) are fitted with a single Gaussian (red dashed line) to derive the centroid velocity (μ) and velocity dispersion (σ). The centroid velocity corresponds to the systematic velocity (V_{lsr}) of the cores, which is marked with vertical-dashed lines in all three panels.

Table 2
Derived Parameters of the Filaments, Inflow Rates, and Mass Transfer of the Filaments Feeding the Hub

Filament ID (1)	L_{fil} (pc) (2)	M_{fil} ($M_\odot$) (3)	m_{fil} ($M_\odot$ pc^{-1}) (4)	$\nabla V_\parallel$ (km s^{-1} pc^{-1}) (5)	$\dot{M}_\parallel$ ($M_\odot$ Myr^{-1}) (6)	$\dot{M}_{\parallel,line}$ ($M_\odot$ Myr^{-1} pc^{-1}) (7)	$\Delta\dot{M}_\parallel$ ($M_\odot$ Myr^{-1}) (8)	ΔM ($M_\odot$) (9)
F1	0.07	99 ± 33	1414 ± 473	17.8 ± 1.1	1762 ± 598	25170 ± 8540	352 ± 120	7.0 ± 2.4
F3	0.13	227 ± 76	1746 ± 585	22.1 ± 2.0	5017 ± 1735	41808 ± 14458	1003 ± 347	20.0 ± 7.0
F4	0.12	119 ± 40	992 ± 333	10.9 ± 0.8	1297 ± 445	10808 ± 3708	259 ± 89	5.2 ± 1.8

Note. (1) Position where the converging flows are measured in Figure 5. (2) Filament length along which the velocity gradient is measured (not corrected for inclination). (3) Filament mass within L_{fil}. (4) Line mass of the filament within L_{fil}. (5) Velocity gradient measured along the filament. (6) Mass inflow rate of the flow motion along the filament by a simple cylindrical model with $\tan\alpha = 1$. (7) Mass inflow rate per unit length. (8) Mass accretion rates assuming an SFE of 20%. (9) Mass gain by the hub in 2×10^4 yr with the adopted SFE.

($13_{1,12}$–$13_{0,13}$) for the protostellar cores (5, 7, and 8), which is a tracer of hot cores, and $H^{13}CN$ (4–3) for the prestellar core candidates (10 and 13). For other prestellar core candidates, we could not obtain the $H^{13}CN$ (4–3) spectra, which might be because of lower flux level and/or significant missing flux. We fit Gaussians to the average spectra of these optically thin tracers to determine the V_{lsr} of each core. Figure 6 shows that the V_{lsr} of these tracers coincides with the dip in the $H^{13}CO^+$ profiles for cores 8, 10, and 13, further confirming that the double-peaked shapes arise from self-absorption and not from a multicomponent cloud. We also compare other infall tracers, such as CS, $H^{13}CN$ (1–0), and CCH, for cores 5 and 7 (Figure C1; Appendix C), which also clearly exhibit infall profiles. Hence, we infer that similar profiles in other cores where no spectrum was obtained for an optically thin tracer also signify the infalling gas. We used the $H^{13}CO^+$ line to analyze the infall motions for the cores. The $H^{13}CO^+$ spectral profiles of protostellar cores and prestellar core candidates are shown separately in Figure 7. As can be seen in Figure 7, protostellar cores 5, 8, and 9 exhibit blue profiles. Among the prestellar candidates, cores 3, 12, 15, and 16 show blue profiles, while cores 10, 11, and 13 show red profiles suggestive of expanding gas.

We also examined the CCH F(2–1) line profile (see Figure 8), which is reported to be a good tracer for infalling gas motions in both prestellar and protostellar cores (M. Padovani et al. 2009; N. Sakai et al. 2010). The line profile of CCH also revealed a similar behavior, i.e., the V_{lsr} obtained from the thin tracers coinciding with the dip in CCH (see Figure 6), with two additional cores showing blue profiles (core 7 in protostellar and core 6 in prestellar candidate). This may be attributed to the high optical thickness of $H^{13}CO^+$ in these regions, which can suppress the blueshifted emission and thereby obscure typical infall signatures (E. M. Gregersen & N. J. Evans 2000). The profiles for all the remaining cores show similar signatures in both the $H^{13}CO^+$ and CCH spectral profiles.

After successful identification of blue profiles, we went on to estimate the infall velocity of the gas in these cores. The infall velocity of the cores with blue profile was determined by fitting the observed spectral profiles of $H^{13}CO^+$ and CCH with the Hill5 infall model (C. H. De Vries & P. C. Myers 2005). This model is developed for deriving infall velocities in a contracting molecular cloud by dealing with radiative transfer processes in two approaching layers whose excitation temperatures linearly increase toward the inner region (see C. H. De Vries & P. C. Myers 2005, for details). To reliably

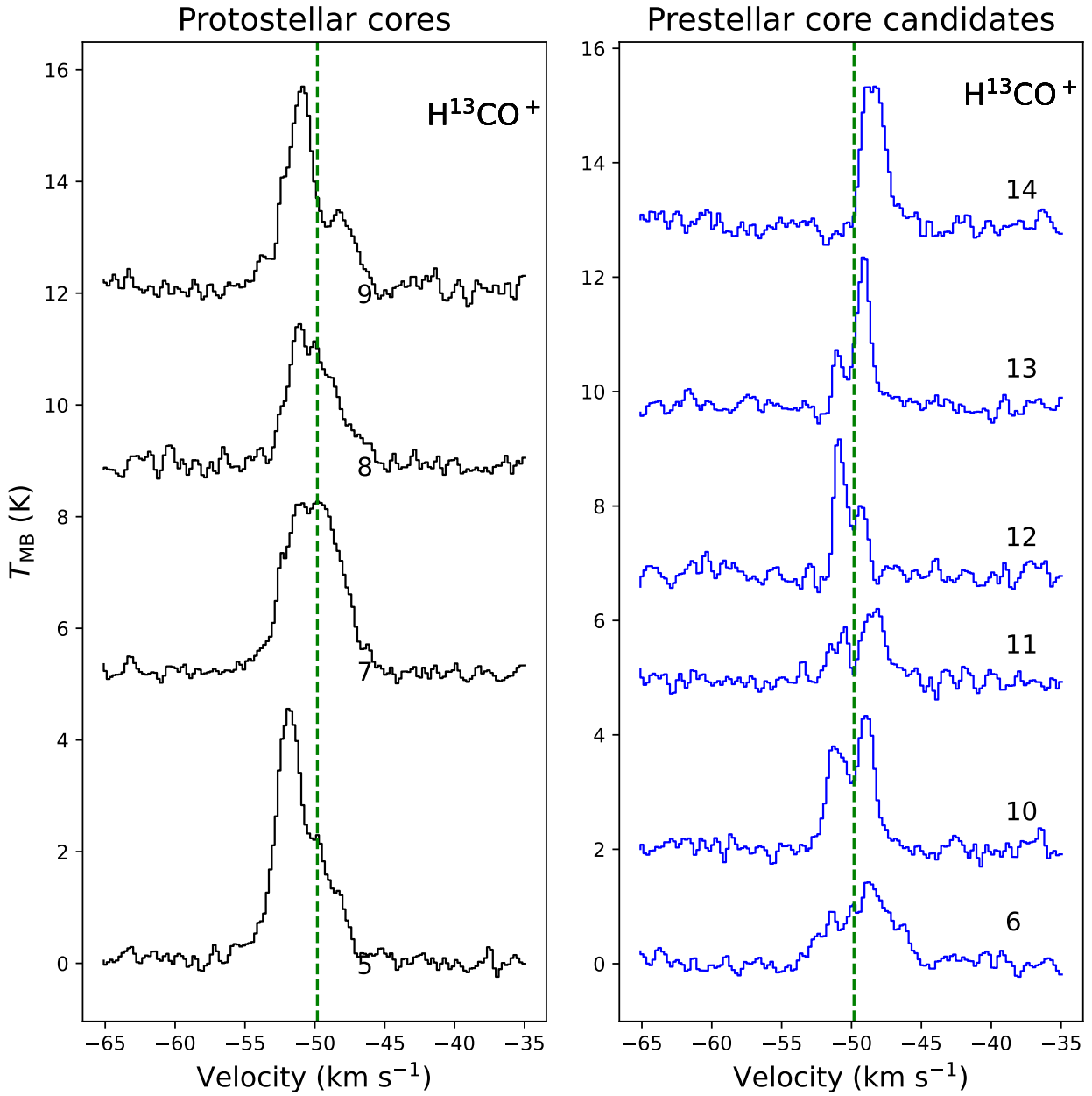

Figure 7. $H^{13}CO^+$ spectra of the protostellar cores (left) and prestellar core candidates (right) in the region. The vertical green line shows the V_{lsr} of the protocluster.

determine the infall velocity from the asymmetric line profiles using the Hill5 model, we applied a signal-to-noise ratio (S/N) threshold $\gtrsim$15 to the observed spectra. The S/N was calculated based on an rms noise level of 0.27 K, estimated from the line-free channels using `FUNStools`.[16]

The overall fitting procedure is summarized in Appendix B, and fitting to the average profile of $H^{13}CO^+$ for core 9 is shown in Figure B1 as an example. The best-fit Hill5 profiles overlaid with the averaged line profiles of $H^{13}CO^+$ and CCH are shown in Figures 9 and 10, respectively. In both figures, the red and blue color fits represent red and blue profiles, respectively. Fit to a few spectra (cores 7, 10, and 14 for $H^{13}CO^+$, and cores 5, 8, 9, 13, and 14 for CCH) were unreliable due to the complex nature of their spectra, and hence, they were excluded from further analysis.

[16] https://github.com/radioshiny/funstools

The resulting infall velocities (V_{in}) are listed in Table 3. By convention, positive V_{in} corresponds to a blue profile, and negative V_{in} indicates a red profile. V_{in} varies from −0.73 to 1.24 km s^{-1} for the cores (see columns (4) and (5) of Table 3). Note that for cores where V_{in} is derived for both the tracers (cores 10, 11, and 12), the obtained values are found to be consistent with each other.

The estimated infall velocities were further used to derive the mass infall rate ($\dot{M}_{in}$) of gaseous material following the equation (e.g., C. W. Lee et al. 2001; S. Kim et al. 2022; S. Moharana et al. 2026):

$$\dot{M}_{in} = \frac{3M_{in}}{R_{in}} V_{in}, \quad (4)$$

where M_{in} is the core mass, and R_{in} is the core radius, adopted from F. Xu et al. (2024a). The calculated values of $\dot{M}_{in}$ are given in Table 3.

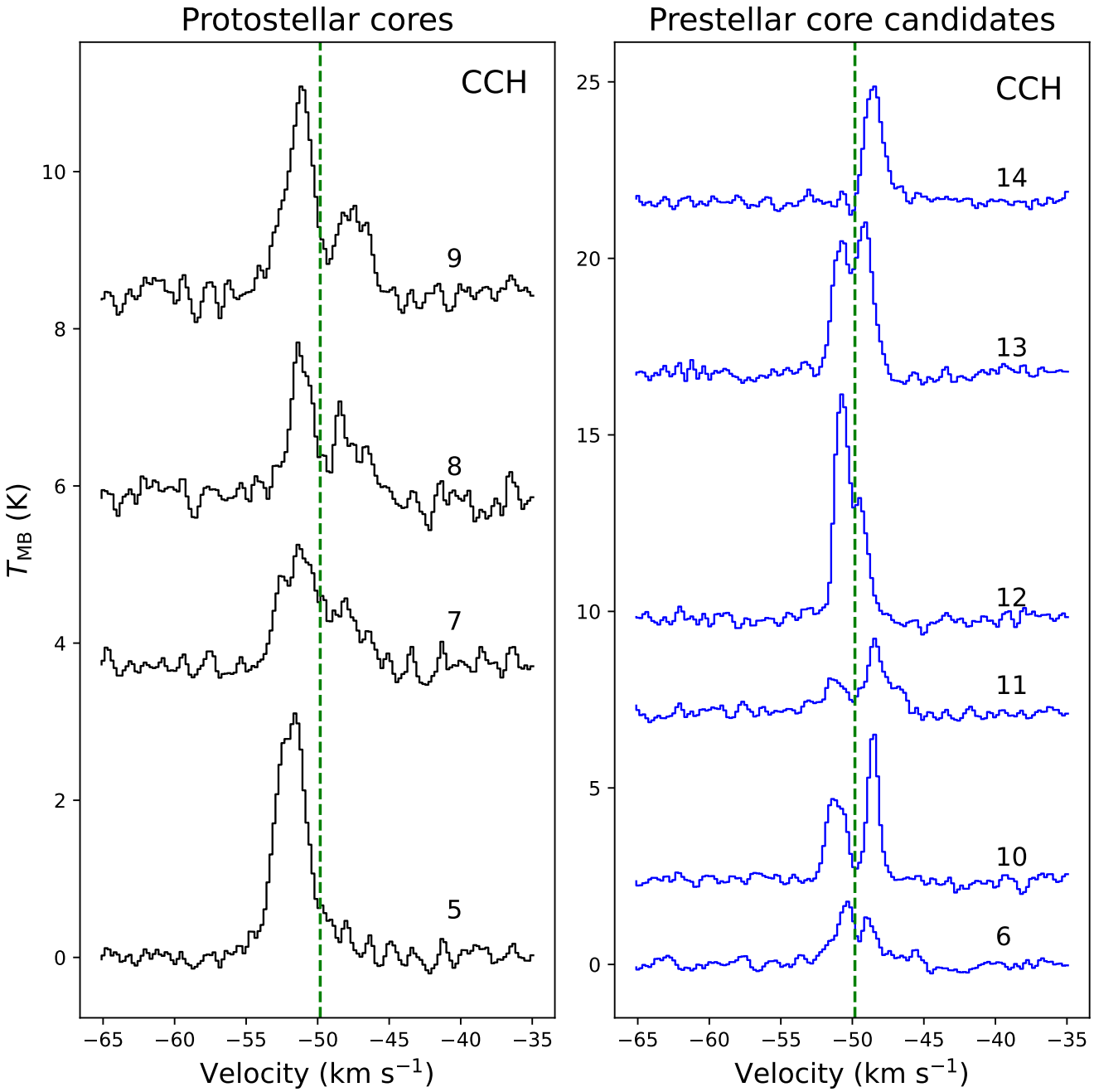

Figure 8. Extracted CCH spectra of the protostellar cores (left) and prestellar core candidates (right). The vertical green line shows the V_{lsr} of the protocluster.

We find that cores located in the hub region, namely, cores 5, 7, 8, and 9, exhibit a high-mass infall rate, with values of 54.9, 196.2, 33.1, and 20.1 $\times$ 10^{-5} $M_{\odot}$ yr^{-1}, respectively. In contrast, cores 10 and 11 (with red profiles) show expansion of gas at a rate of 68.9 and 39.3 $\times$ 10^{-5} $M_{\odot}$ yr^{-1}, respectively. Other cores exhibit comparatively lower infall rates, consistent with their peripheral positions and possibly earlier evolutionary stages (see Section 4.4 for further discussion).

4. Discussion

In Section 3, we found that there exist at least four filaments that show evidence of carrying gas to the central hub where multiple star-forming cores are present. Also, these filaments are inflowing gas at a rate of more than 10^3 $M_{\odot}$ Myr^{-1}. With such a high gas inflow rate, these filaments are capable of transporting enough gas to the central hub for the formation of massive stars. In fact, all the cores located at the central hub are showing the signature of infalling gas. In this section, we discuss our overall analyses in terms of the star formation activity in the protocluster.

4.1. Mass–Radius Relation of the Cores

To further examine the star-forming nature of the cores, we analyzed their mass–radius relation, which provides important clues as to whether a core will evolve into a massive star or into a low-mass star. The mass–radius relation of all the identified cores in this protocluster is shown in Figure 11. The shaded region represents the area of low-mass star-forming cores that do not satisfy the criteria of $m(r) > 870\,M_{\odot}\,(r/\mathrm{pc})^{1.33}$ (J. Kauffmann et al. 2013). It highlights the

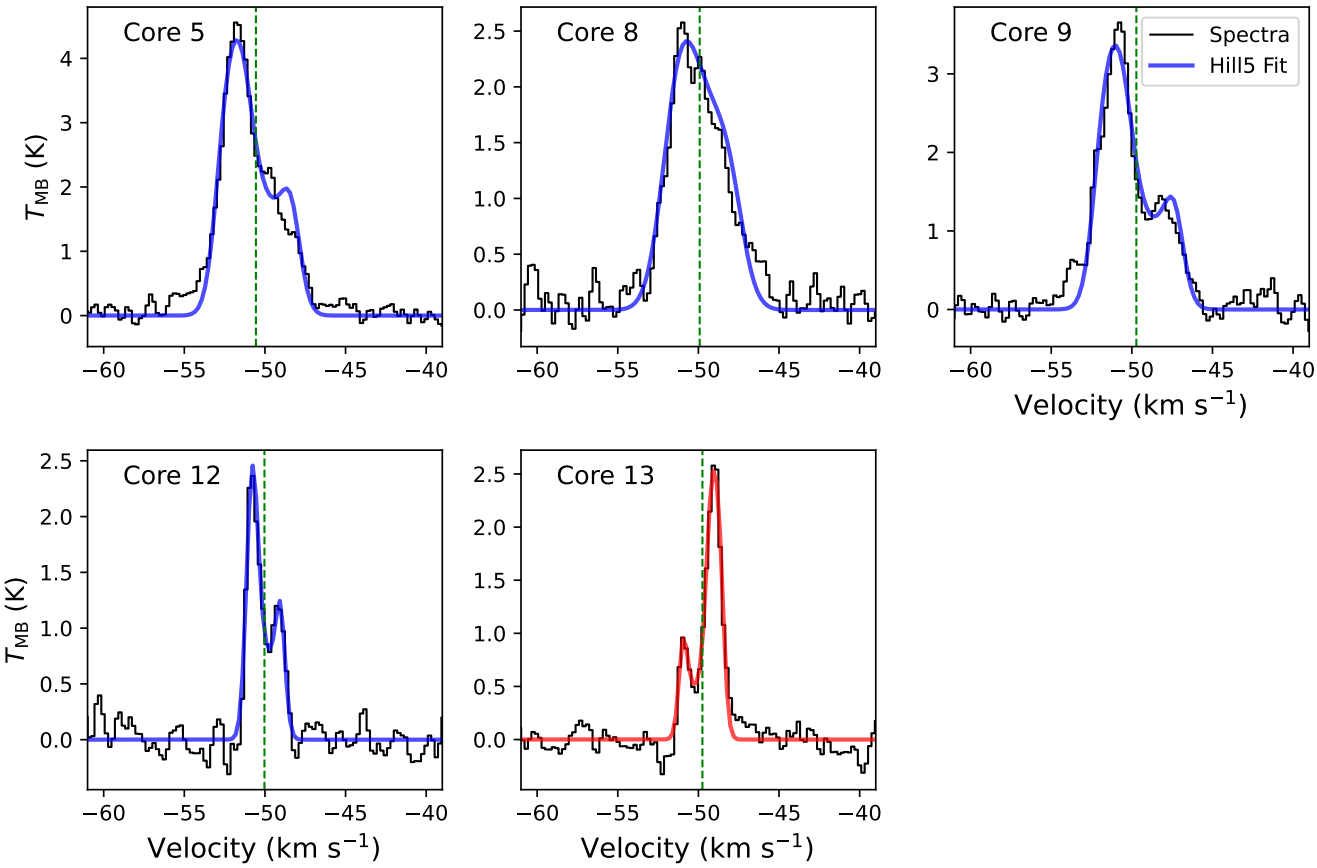

Figure 9. Model fit to the $H^{13}CO^{+}$ spectral profiles (shown in black) of the cores. The profiles show the best-fit results with the Hill5 model (C. H. De Vries & P. C. Myers 2005). Model fitted spectra to the blue profiles are shown in blue color, while the fit to the red profile is shown in red color. The green dashed lines show the V_{lsr} of each core derived from Hill5.

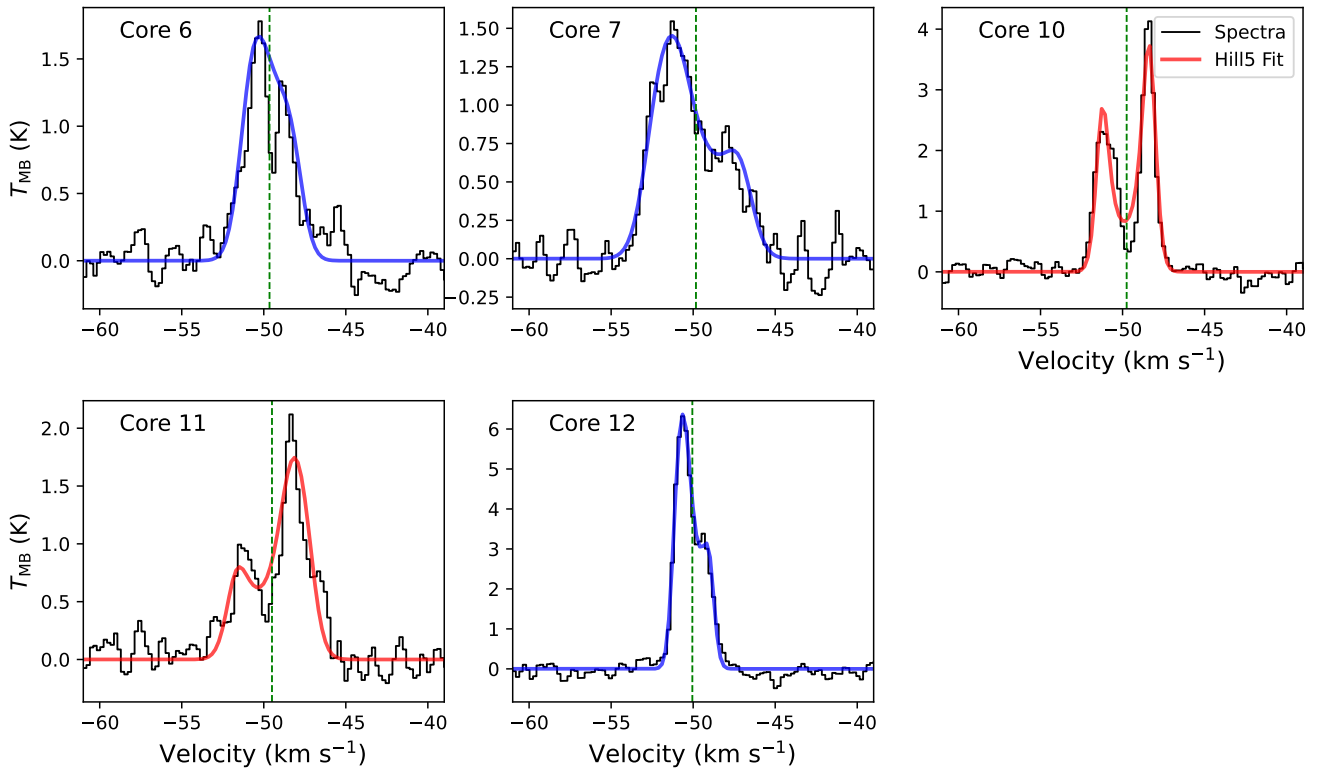

Figure 10. Model fit to the CCH spectral profiles (shown in black) of the cores. The remaining symbols are the same as those in the caption of Figure 9.

Table 3
Estimated Physical and Dynamical Parameters of the Cores

Core ID	Mass	Radius	$V_{\rm lsr}$	$V_{\rm in}(H^{13}CO^+)$	$V_{\rm in}$(CCH)	$\dot{M}_{\rm in}(H^{13}CO^+)$	$\dot{M}_{\rm in}$(CCH)
	($M_\odot$)	(au)	(km s^{-1})	(km s^{-1})	(km s^{-1})	($\times10^{-5}$ $M_\odot$ yr^{-1})	($\times10^{-5}$ $M_\odot$ yr^{-1})
(1)	(2)	(3)	(4)	(5)	(6)	(7)	(8)
5	4.0 ± 2.4	4550	−50.61	$1.05^{+0.12}_{-0.11}$	⋯	54.9 ± 35.1	⋯
6	0.9 ± 0.7	4840	⋯	⋯	$0.56^{+0.28}_{-0.31}$	⋯	6.6 ± 5.1
7	9.7 ± 5.2	3680	−50.70	⋯	$1.24^{+0.26}_{-0.27}$	⋯	196.2 ± 110.9
8	1.0 ± 0.6	1530	−50.18	$0.80^{+0.16}_{-0.18}$	⋯	33.1 ± 19.9	⋯
9	1.0 ± 0.6	3740	⋯	$1.08^{+0.10}_{-0.10}$	⋯	20.1 ± 11.0	⋯
10	6.0 ± 4.1	3360	−49.31	$-0.16^{+0.06}_{-0.07}$	$-0.14^{+0.03}_{-0.03}$	−68.9 ± 41.7	−46.3 ± 31.7
11	1.3 ± 1.0	1530	⋯	$-0.73^{+0.32}_{-0.56}$	$-0.73^{+0.18}_{-0.32}$	−39.3 ± 30.2	⋯
12	1.1 ± 0.8	3770	⋯	$0.44^{+0.08}_{-0.06}$	$0.45^{+0.11}_{-0.07}$	5.0 ± 3.6	⋯
13	1.3 ± 0.9	1530	−50.30	$-0.49^{+0.08}_{-0.10}$	⋯	−26.4 ± 18.2	⋯
14	5.5 ± 3.5	3740	⋯	⋯	⋯	⋯	⋯

Note. (1): core IDs. (2) and (3): mass and radius of the cores, respectively, as adopted from F. Xu et al. (2024a). (4): $V_{\rm lsr}$ of each core derived from thin tracer CH_3OH ($13_{1,12}$–$13_{0,13}$) and $H^{13}CN$ (4–3). (5) and (6): infall velocities of the cores derived using the Hill5 model from the average spectra of $H^{13}CO^+$ and CCH, respectively. (7) and (8): mass infall rates for each of the cores derived from $V_{\rm in}(H^{13}CO^+)$ and $V_{\rm in}$(CCH), respectively; here, negative mass infall rates correspond to expansion.

domain where low-mass cores are typically found, bounded below by the gravitational binding limit of $\Sigma = 0.05$ g cm^{-2} (M. R. Krumholz & C. F. McKee 2008). Most of the cores lie below the critical surface density of $\Sigma = 1.0$ g cm^{-2} (J. S. Urquhart et al. 2014), suggesting they are associated with low-mass star formation.

The protostellar core, core 7, residing in the hub region, exceeds both the surface density threshold and the 8 $M_\odot$ mass limit, making it a potential candidate to evolve into a massive star. Note that cores 10, 11, and 14 also lie in the massive star formation regime but exhibit red profiles, indicating ongoing mass-loss or mass redistribution possibly to the central hub. To investigate this further, we look into the dynamical properties of the host filaments (F3 and F4) of the cores 10 and 11, as it is important to assess gas dynamics and understand the potential mass transfer toward the hub.

4.2. Velocity Variation along the Filament

Velocity and density fluctuations along filaments are noted in several studies (S. Kim et al. 2022; J.-W. Zhou et al. 2022). Such fluctuations are likely caused by dense structures (i.e., cores) embedded within the filaments (H.-L. Liu et al. 2019). Fluctuations along filaments may indicate oscillatory gas flows coupled to regularly spaced density enhancements that probably form via gravitational instabilities (J. D. Henshaw et al. 2020). Figure 12 presents the intensity and the velocity distribution (i.e., PV) along the filaments in this protocluster, including the hub starting from F3 to F4. The velocity distribution exhibits a global minimum (lower panel), which spatially coincides with the peak of the integrated $H^{13}CO^+$ intensity (upper panel), corresponding to the center of the gravitational potential well (i.e., the hub region). Clear velocity gradients can be noted on both sides of this hub region (see Figure 5), and the corresponding gradients were estimated in Section 3.3.

The positions of the cores are marked by vertical-dashed lines in Figure 12, with blue dotted–dashed lines representing the cores within the hub region, red and blue dashed lines denoting cores exhibiting red and blue-asymmetric spectral profiles, and pink corresponding to the rest of the cores that lie along filaments F3 and F4. A clear shallow dip in the velocity profile is observed at the centroid position of core 11, while

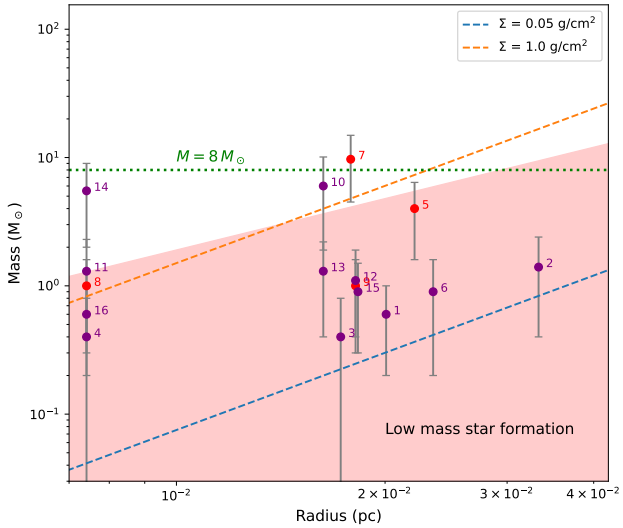

Figure 11. The radii vs. masses of the cores. The red circles mark the protostellar cores, while the purple circles represent the prestellar core candidates. The shaded region represents the area of low-mass star-forming cores that do not satisfy the criteria of $m(r) > 870\,M_\odot\,(r/\mathrm{pc})^{1.33}$. Surface density thresholds of 0.05 and 1 g cm^{-2} are shown as blue and orange dashed lines, respectively. The green dotted line is for a core mass of 8 $M_\odot$.

core 10 is located on a steep velocity gradient, and both cores are located at minima in integrated intensity, suggesting their dynamical connection with the hub region, i.e., cores 10 and 11 are not gathering a significant amount of the mass. Note that such a scenario is typically expected for competitive accretion theory, in which several cores/condensations are expected to create the global potential to transport gas from the outer part to its gravitational center (i.e., hub), and feed the cores residing in the hub.

4.3. Possible Evolution of the Cores

The high velocity gradient and large mass inflow rates (on the order of 10^4 $M_\odot$ Myr^{-1}) toward the hub suggest that these filaments are actively feeding material into the central hub, where the protostellar cores reside. Such inflow can lead to rapid evolution of cores in the hub, potentially supporting massive star formation. A high infall rate exceeding

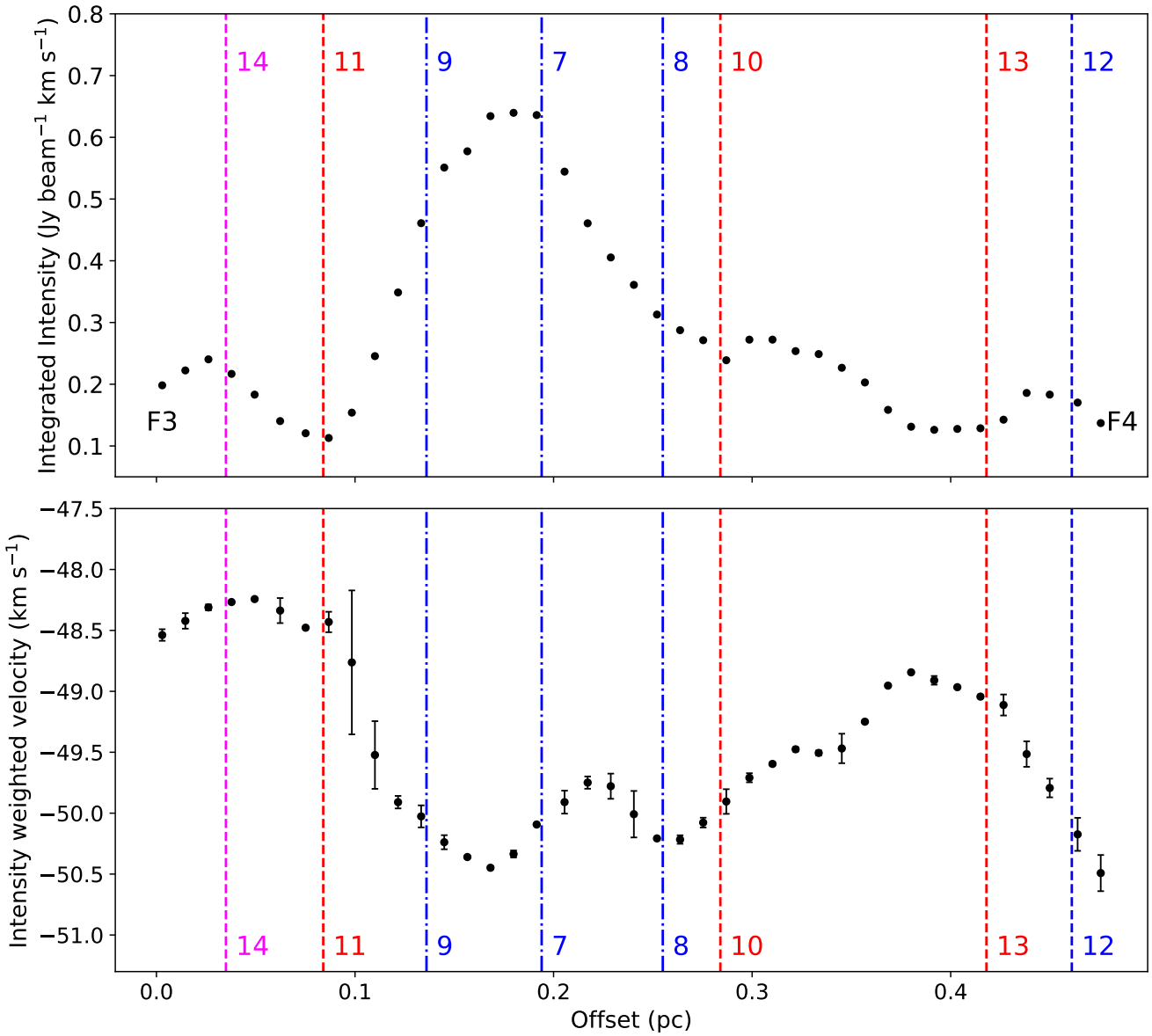

Figure 12. The upper panel shows the distributions of integrated intensity along filament F3-F4, while the lower panel displays the intensity-weighted velocity (PV) along the same filament using $H^{13}CO^{+}$(see Figure 4). In both panels, the values are uniformly sampled along the filament skeletons following the same methodology as described in Figure 5. The velocity error bars represent the standard deviation of the velocities within each sampled bin along the offset. Blue and red vertical lines indicate the positions of dense cores with blue and red profiles, respectively, residing along the filament, whereas the magenta vertical line shows the position of the dense core with a single-peaked profile. The dotted–dashed vertical blue lines in the central part show the positions of the cores associated with the hub.

$\sim$1000 $M_{\odot}$ Myr^{-1} is typically required to form massive stars before radiative feedback halts further growth (C. F. McKee & J. C. Tan 2003).

S. D. Doty et al. (2002) estimate that the chemical timescale relevant for massive star formation ranges between 7×10^3 and 5×10^4 yr, with a characteristic timescale of approximately 3×10^4 yr. Similarly, M. R. Krumholz et al. (2009) suggest that protostellar accretion proceeds smoothly over a period of roughly 2×10^4 yr. Accumulation of a small fraction ($\sim$20%–30%) of inflowing gas (see Table 2) onto the individual core during this timescale may lead to a significant mass growth and potentially lead to the formation of massive stars or a stellar cluster. This fractional conversion of inflowing mass into stellar mass is commonly quantified as the star formation efficiency (SFE). C. D. Matzner & C. F. McKee (2000) proposed SFE values in the range of 30%–50% for clustered low-mass star-forming regions and considered this range to represent upper limits for high-mass environments. Additionally, J. Alves et al. (2007) suggested a uniform SFE of 30% $\pm$ 10%, consistent with the observed shape of the stellar initial mass function (IMF).

For example, F3 has an inflow rate of 5135 $M_{\odot}$ Myr^{-1}. A core in the hub region with a typical 20% accumulation efficiency of gas transportation rate of F3 can gain $\sim$20 $M_{\odot}$ in just 20,000 yr (M. R. Krumholz et al. 2009), which is substantial, especially when it already had a seed mass. Columns (8) and (9) of Table 2 list the mass inflow rates of the filaments (see Section 3.3), a value of fractional mass inflow rate to the core assuming an efficiency of 20%, and an estimation of the core mass that accumulates over a timescale of 2×10^4 yr with this effective mass inflow.

With a typical conjecture of mass inflow through the filaments 2×10^4 yr at a constant efficiency of 20%, the additional mass accreted by the hub would rise by 35 $M_{\odot}$,

while it would increase by 52.5 $M_\odot$ if an efficiency of 30% is assumed. In both cases, the accumulated mass is sufficient to form massive stars within the hub.

4.4. Infall and Inflow Rates: An Overview

The global infall rate of $(1.56 \pm 0.03) \times 10^4$ $M_\odot$ Myr^{-1}, estimated at a radius of 0.74 pc using the CO (4–3) line by Y.-H. Yue et al. (2021) provide a large-scale view of accretion in this system. Zooming into a smaller scale, around 0.3 pc, we observe the individual filamentary structures feeding the central hub.

For filament F4, the inflow rate is estimated to be 1297 $M_\odot$ Myr^{-1}. Core 12, located at the periphery of this filament, shows a small infall rate of ∼50 $M_\odot$ Myr^{-1} (∼3% of the total inflow). Notably, as we move toward the hub region along the filament, core 13 and core 10 appear to be losing mass (with a negative infall rate of ∼260 and ∼500 $M_\odot$ Myr^{-1}, respectively), possibly contributing material to the central hub (core 8). These increasing negative infall rates are suggestive of increasing gravitational potential toward the hub. Within the hub region, core 8 exhibits the highest infall rate of 330 $M_\odot$ Myr^{-1}, accounting for ∼25% of the total inflow—highlighting significant mass accumulation at the hub.

For filament F3, the estimated inflow rate is 5017 $M_\odot$ Myr^{-1}. Core 14 shows no significant accretion activity. Moving toward the hub along the filament, core 11 appears to be losing mass at a rate of approximately 400 $M_\odot$ Myr^{-1}, likely feeding core 9, which itself is accreting at an infall rate of 200 $M_\odot$ Myr^{-1}. The contribution from the filament F3 is approximately 4% to the core 9. For filament F1, the inflow rate is estimated to be 1762 $M_\odot$ Myr^{-1}. Core 5 is collapsing with an infall rate of 550 $M_\odot$ Myr^{-1}, which corresponds to approximately 31% of the mass being supplied by the filament. Core 7 has the highest infall rate of 1962 $M_\odot$ Myr^{-1}. With all three filaments feeding material to this core together, this corresponds to 25% of the combined inflow rate. It shows that in the hub region, the infall rate is very high (4%–27%) compared to the total inflow rate of their respective filaments. Note that all these calculations are done in the immediate vicinity of the adjacent filament.

These results collectively demonstrate a hierarchical mass accretion structure: at larger scales ($R \sim 0.74$ pc), the accretion rate is on the order of 10^4 $M_\odot$ Myr^{-1}; at filament scales (∼0.3 pc), it drops to 10^3 $M_\odot$ Myr^{-1}; and at core scales, further down to 10^2 $M_\odot$ Myr^{-1}. This progression strongly supports the hub–filament paradigm, where gravitational potential wells at the hub center govern the mass flow. The increasing inflow toward the hub and the transition from low infall in peripheral cores to enhanced accretion in inner cores illustrate the dynamic, gravity-driven nature of star-forming environments.

5. Summary

We investigated the massive protocluster G318.049+00.086, utilizing molecular line and continuum data from the ATOMS, ASSEMBLE, and QUARKS surveys. This region has been identified as a hub-filament system. Recently, F. Xu et al. (2024a) reported the presence of 16 cores within this protocluster, comprising four protostellar and 12 prestellar core candidates, with the protostellar ones concentrated in the hub region.

Using $H^{13}CO^+$ and CCH spectral line data, along with 1.3 mm continuum emission, we explored the gas dynamics of the embedded cores and the role of filamentary structures in the formation and evolution of these cores. Our main findings are summarized below:

1. The 1.3 mm continuum with higher spatial resolution reveals four filaments in the densest regions covering the hub and its vicinity. These filaments (F1–F4) spatially coincide with the cores near the hub region.
2. The H_2 column density map was derived from the N($H^{13}CO^+$) column density map. While the estimated filament masses are typical for galactic filaments, about 100 $M_\odot$, the estimated line masses of the filaments are found to be 992–1746 $M_\odot$ pc^{-1}, which are typical for giant filaments.
3. The velocity gradients along filaments F1, F3, and F4 were 17.8, 22.1, and 10.9 km s^{-1}, respectively, and the corresponding mass inflow rates were 1762, 5017, and 1297 $M_\odot$ yr^{-1}.
4. The cores associated with the protocluster show blue- and red-asymmetric line profiles in both $H^{13}CO^+$ and CCH spectra, indicative of infalling and expanding gas. Interestingly, the majority of the protostellar cores show blue profiles, a signature of infalling gas. A few prestellar core candidates located on the filaments showed red profiles. Infall velocities were determined using the Hill5 model fits with Markov Chain Monte Carlo (MCMC) sampling, yielding mass infall rates of approximately $\sim(7–196) \times 10^{-5}$ $M_\odot$ Myr^{-1}.
5. The mass–radius relation suggests that while most cores lie in the low-mass star formation regime, those situated in the high-mass regime predominantly show red profiles. This scenario possibly signifies that although they have the potential to form a massive star, they are significantly losing their mass either in the form of expansion or to feed the central hub. In fact, PV analysis confirms that two of these cores are funneling mass into the hub region, supporting the competitive accretion scenario.
6. The mass inflow rates along the filaments are consistently higher than the core-level infall rates, suggesting an ongoing and efficient mass supply mechanism from large to small scales. If the filamentary accretion continues uninterrupted, the central hub is expected to accumulate sufficient mass to support the formation of massive stars.

Acknowledgments

We thank the anonymous referee for the constructive comments and suggestions. G.G. gratefully acknowledges the support of the ANID BASAL project FB210003. A.H. gratefully acknowledges the support of the S. N. Bose National Centre for Basic Sciences under the Department of Science and Technology, Government of India, and the CSIR-HRDG, Government of India, for the funding of the fellowship. C.W.L. is supported by the Basic Science Research Program through the National Research Foundation of Korea (NRF) funded by the Ministry of Education, Science and Technology (grant No. NRF-2019R1A2C1 010851), and by the Korea Astronomy and Space Science

Institute grant funded by the Korean government (MSIT; project No. 2025-1-841-02).

Appendix A
Moment 0 Map of All Line Tracers in ATOMS

To show the comparison between all the molecular lines, we have overplotted all the cores on the velocity-integrated intensity map (see Figure A1).

The moment 0 maps reveal that many of the molecular tracers, including HCN, HCO^+, CS, and CH_3OH, peak toward the core positions, showing strong spatial correlation with the 3 mm continuum. This suggests that these lines are closely associated with ongoing star formation activity. In contrast, tracers like CS, SO, and SiO show the spatial correlation by showing the shock region and tracing the same nodes. HCN and HCO^+ show a similar correlation and trace the outflow activity. $H^{13}CN$, $H^{13}CO^+$, and CCH F(2-1) show a spatial correlation and trace the same denser region.

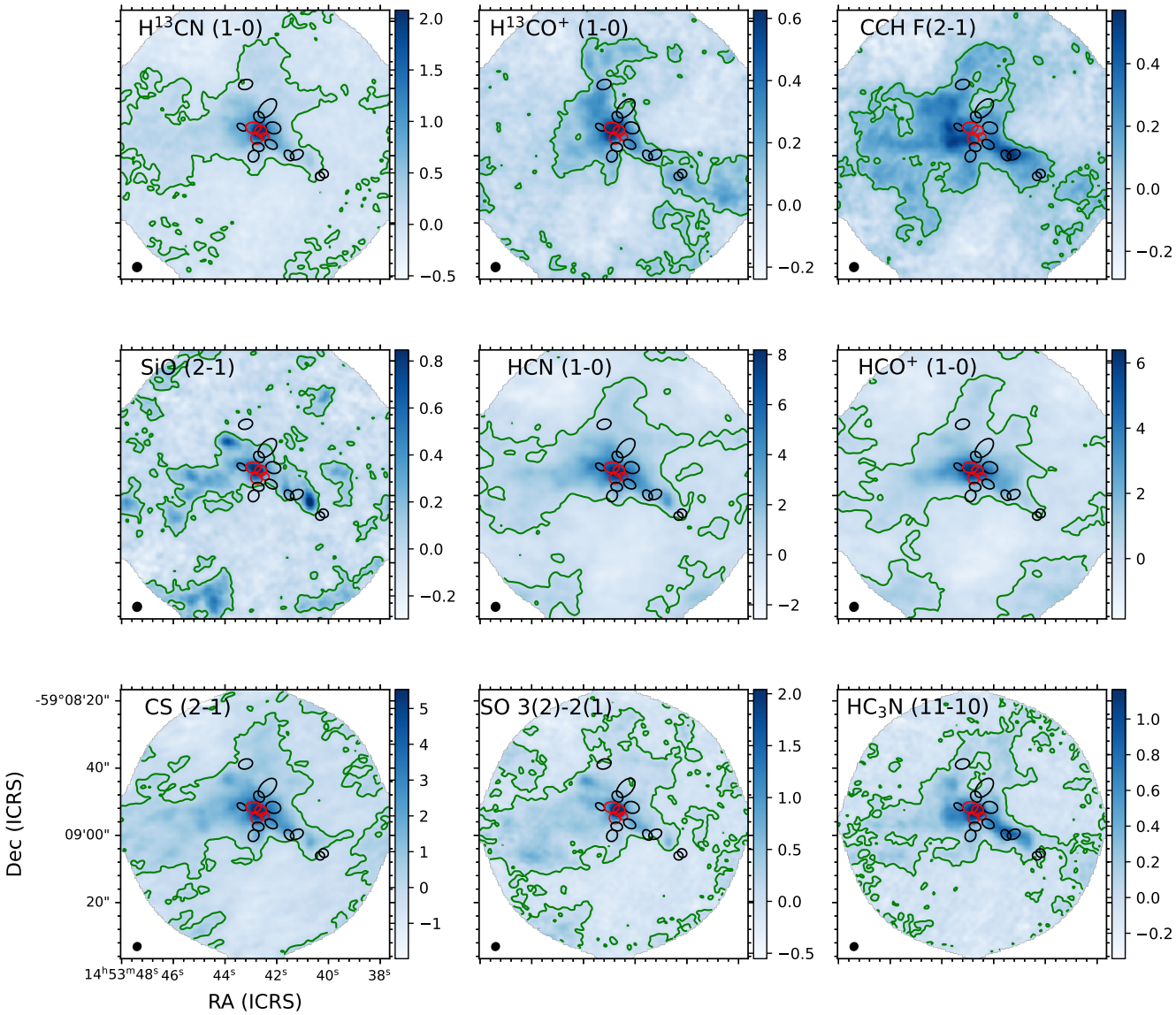

Figure A1. Moment 0 maps of the molecular transitions observed toward G318.049+00.086. The beam sizes are shown in black at the left corner of each subplot. The color bars indicate integrated intensities in units of Jy beam^{-1} km s^{-1}. The ellipses represent the adopted cores at 870 μm by F. Xu et al. (2024a). Red and black ellipses denote protostellar cores and prestellar core candidates, respectively. Green contours are drawn at the 5σ level. The σ values for the individual transitions are 10.2, 11.1, 11.7, 10.9, 15.7, 16.1, 4.8, 5.1, and 5.2 Jy beam^{-1} km s^{-1}, respectively, following the panel order.

Appendix B
Hill5 Model Fit to the Infall Profiles

The Hill5 model is a simple radiative transfer model used for deriving infall velocity in a contracting molecular cloud by dealing with radiative transfer processes in two approaching layers whose excitation temperatures linearly increase toward the inner region (see Equation (9) of C. H. De Vries & P. C. Myers 2005). The model consists of a core with a peak excitation temperature ($T_{\rm peak}$) at the center and an excitation temperature of $T_0 = 0$ at the near and far edges of the core. The optical depth of the core is τ, and its infall velocity is $V_{\rm infall}$, while the systematic velocity of the system is $V_{\rm lsr}$, and both regions are assumed to have equal velocity dispersion of σ for the observed molecule. These five parameters were set as free with initial guesses and bounds to fit the observed spectra with the model.

For robust fitting with accurate estimation of the error of fitted parameters, the fitting was performed by MCMC sampling using the `emcee`[17] Python package (D. Foreman-Mackey et al. 2013). The corner plots were generated to check the posterior probability distributions of parameters for each

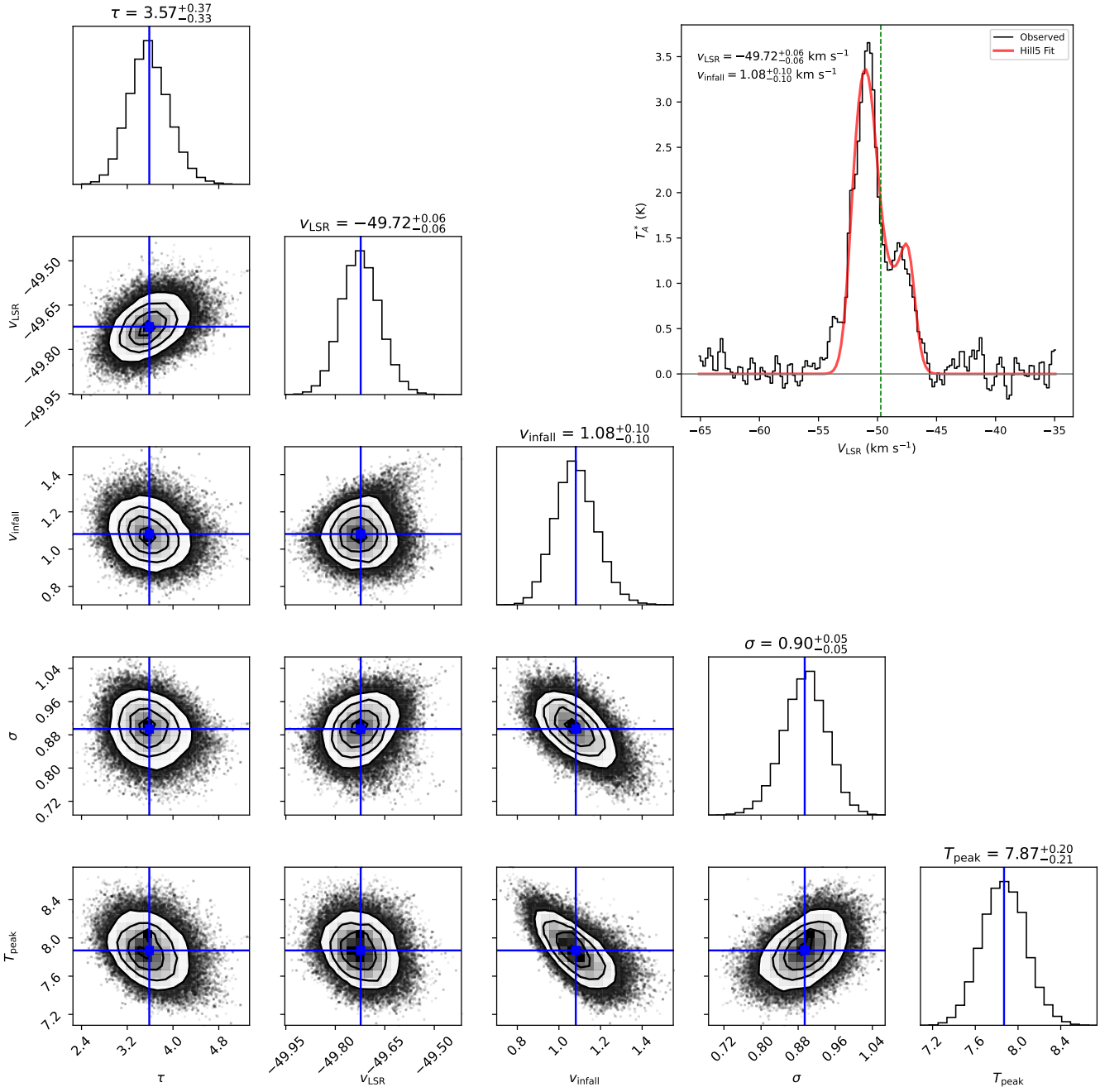

Figure B1. Determination of infall velocity and local standard of rest velocity of core 9. The corner plots show the posterior probability distributions of parameters. The blue lines show the median values of the parameters. The best-fit model (red line) is overplotted on the average spectra (black line) at the upper-right corner of the figure. The vertical green dashed line marks the obtained $V_{\rm lsr}$ from the fit.

[17] https://github.com/dfm/emcee

spectrum. In the initial trial, we set the parameter range very broad to identify the most probable region across possible local minima. The second trial uses this result to set more reasonable bounds on the parameters for a final fit. Figure B1 shows the posterior distribution of the parameters in the second trial, as well as the final fit to the spectra of core 9.

Appendix C
Spectral Profiles of Core 5 and Core 7

Figure C1 presents the averaged spectral profiles of various molecular tracers for core 5 (left) and core 7 (right). The optically thin CH_3OH ($13_{1,12}$–$13_{0,13}$) line is fitted with a single Gaussian profile to determine the centroid velocity (μ) and velocity dispersion (σ), where μ represents the systemic velocity (V_{lsr}) of the core. Comparison with other tracers, including $H^{13}CO^+$, CS, $H^{13}CN$ (1–0), and CCH, reveals clear evidence of infall signatures in both cores. The $H^{13}CN$ (1–0) transition exhibits three hyperfine components, with the main component having an offset from $V_{lsr,}$ which also shows a signature of infall in both. For core 5, the derived V_{lsr} lies near the self-absorption dip between the blue and red peaks of $H^{13}CO^+$ and CS line profiles, indicating the ongoing infall motions, while the CCH emission also exhibits a similar displacement between its peak intensity and V_{lsr}. These characteristics collectively suggest that the observed line asymmetries are primarily caused by infall motions rather than the presence of multiple velocity components along the line of sight. For core 7, located in the most dense hub region, a shallow dip is seen in the $H^{13}CO^+$ profile, while CCH shows a more prominent blue asymmetry. Although the CCH dip does not coincide exactly with V_{lsr}, it is offset from the line peak; considering all tracers together, we interpret this as indicative of infall activity in the core.

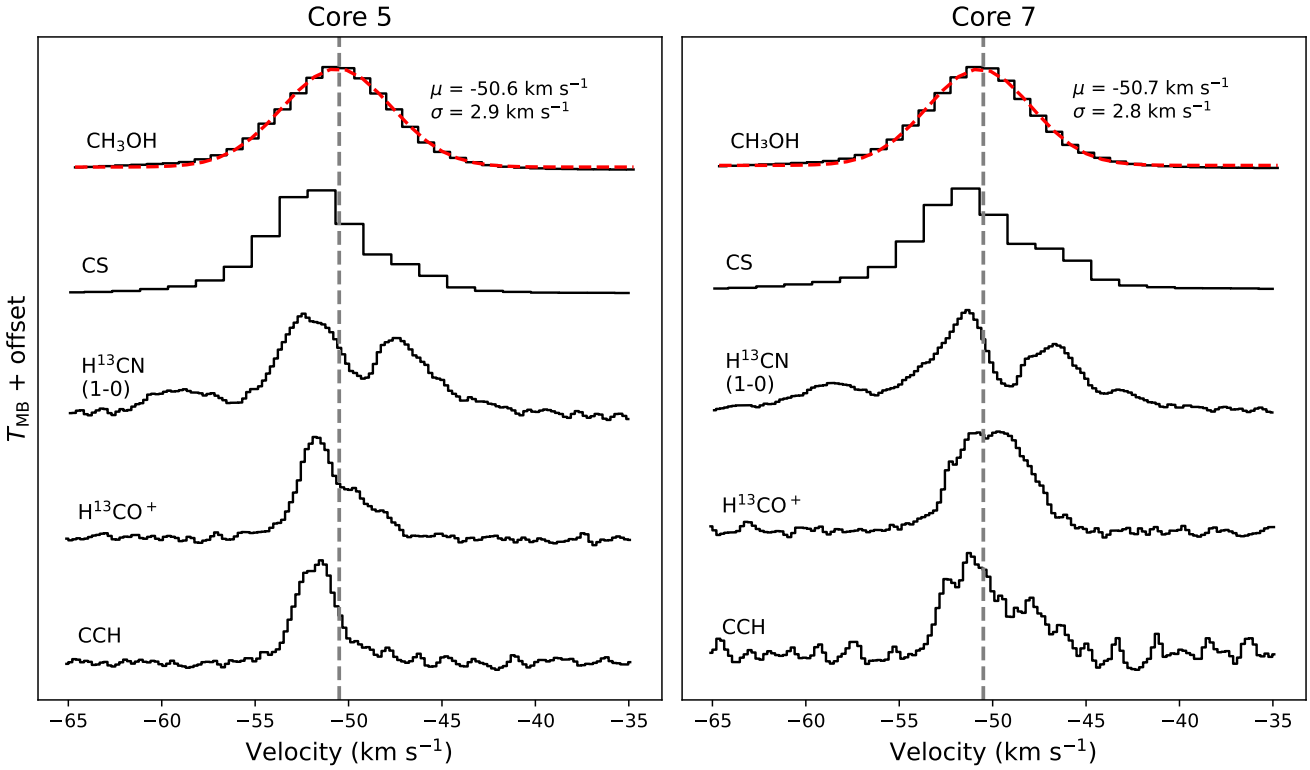

Figure C1. The average spectra of CH_3OH ($13_{1,12}$–$13_{0,13}$) and other infall tracers for cores 5 (left) and 7 (right). The CH_3OH ($13_{1,12}$–$13_{0,13}$) line is fitted with a single Gaussian as shown in red color. The fitted line centroid velocity (μ), i.e., the V_{lsr} of the core and the velocity dispersion (σ) are shown on the right. The vertical gray dashed line marks the obtained V_{lsr} from the fit.

ORCID iDs

Shivani Gupta https://orcid.org/0000-0002-8614-0025
Tapas Baug https://orcid.org/0000-0003-0295-6586
Archana Soam https://orcid.org/0000-0002-6386-2906
Tie Liu https://orcid.org/0000-0002-5286-2564
Fengwei Xu https://orcid.org/0000-0001-5950-1932
Satyajeet Moharana https://orcid.org/0009-0007-9411-0284
Guido Garay https://orcid.org/0000-0003-1649-7958
Chang Won Lee https://orcid.org/0000-0002-3179-6334
Siju Zhang https://orcid.org/0000-0002-9836-0279
Ariful Hoque https://orcid.org/0009-0003-6633-525X
Puja Porel https://orcid.org/0009-0002-6147-531X
Dongting Yang https://orcid.org/0009-0004-6159-5375
HongLi Liu https://orcid.org/0000-0003-3343-9645
Wenyu Jiao https://orcid.org/0000-0001-9822-7817
Xunchuan Liu https://orcid.org/0000-0001-8315-4248
Alik Panja https://orcid.org/0000-0002-4719-3706
Xiaofeng Mai https://orcid.org/0000-0001-7573-0145
Yankun Zhang https://orcid.org/0000-0001-7817-1975
Shinyoung Kim https://orcid.org/0000-0001-9333-5608

References

Alves, J., Lombardi, M., & Lada, C. J. 2007, A&A, 462, L17
Ballesteros-Paredes, J., Hartmann, L. W., Vázquez-Semadeni, E., Heitsch, F., & Zamora-Avilés, M. A. 2011, MNRAS, 411, 65
Baug, T., Wang, K., Liu, T., et al. 2020, ApJ, 890, 44
Blake, G. A., Sutton, E. C., Masson, C. R., & Phillips, T. G. 1987, ApJ, 315, 621
Bonnell, I. A., & Bate, M. R. 2006, MNRAS, 370, 488
Bonnell, I. A., Bate, M. R., Clarke, C. J., & Pringle, J. E. 1997, MNRAS, 285, 201
Bonnell, I. A., Bate, M. R., Clarke, C. J., & Pringle, J. E. 2001, MNRAS, 323, 785
Bonnell, I. A., Larson, R. B., & Zinnecker, H. 2007, in Protostars and Planets V, ed. B. Reipurth, D. Jewitt, & K. Keil (Univ. Arizona Press), 149
Botschwina, P., Horn, M., Flügge, J., & Seeger, S. 1993, FaTr, 89, 2219
Camacho, V., Vázquez-Semadeni, E., Palau, A., Busquet, G., & Zamora-Avilés, M. 2020, ApJ, 903, 46
De Vries, C. H., & Myers, P. C. 2005, ApJ, 620, 800
De Vries, C. H., Narayanan, G., & Snell, R. L. 2002, ApJ, 577, 798
Doty, S. D., van Dishoeck, E. F., van der Tak, F. F. S., & Boonman, A. M. S. 2002, A&A, 389, 446
Foreman-Mackey, D., Conley, A., Meierjurgen Farr, W., et al. 2013, emcee: The MCMC Hammer, Astrophysics Source Code Library, ascl:1303.002
Frerking, M. A., Langer, W. D., & Wilson, R. W. 1987, ApJ, 313, 320
García-Burillo, S., Martín-Pintado, J., Fuente, A., & Neri, R. 2000, A&A, 355, 499
Garden, R. P., Hayashi, M., Gatley, I., Hasegawa, T., & Kaifu, N. 1991, ApJ, 374, 540
Gregersen, E. M., & Evans, N. J., II 2000, ApJ, 538, 260
Hacar, A., Clark, S. E., Heitsch, F., et al. 2023, ASPC, 534, 153
Handa, T., Sakano, M., Naito, S., Hiramatsu, M., & Tsuboi, M. 2006, ApJ, 636, 261
Henshaw, J. D., Kruijssen, J. M. D., Longmore, S. N., et al. 2020, NatAs, 4, 1064
Kauffmann, J., Pillai, T., & Zhang, Q. 2013, ApJL, 765, L35
Kim, S., Lee, C. W., Tafalla, M., et al. 2022, ApJ, 940, 112
Kirk, H., Myers, P. C., Bourke, T. L., et al. 2013, ApJ, 766, 115
Koch, E. W., & Rosolowsky, E. W. 2015, MNRAS, 452, 3435
Krumholz, M. R., Klein, R. I., & McKee, C. F. 2007, ApJ, 656, 959
Krumholz, M. R., Klein, R. I., McKee, C. F., Offner, S. S. R., & Cunningham, A. J. 2009, Sci, 323, 754
Krumholz, M. R., & McKee, C. F. 2008, Natur, 451, 1082
Krumholz, M. R., & Tan, J. C. 2007, ApJ, 654, 304
Kumar, M. S. N., Palmeirim, P., Arzoumanian, D., & Inutsuka, S. I. 2020, A&A, 642, A87
Lattanzi, V., Walters, A., Drouin, B. J., & Pearson, J. C. 2007, ApJ, 662, 771
Lee, C. W., Myers, P. C., & Tafalla, M. 2001, ApJS, 136, 703
Liu, H.-L., Stutz, A., & Yuan, J.-H. 2019, MNRAS, 487, 1259
Liu, T., Evans, N. J., Kim, K.-T., et al. 2020, MNRAS, 496, 2790
Liu, T., Kim, K.-T., Yoo, H., et al. 2016, ApJ, 829, 59
Liu, X., Liu, T., Zhu, L., et al. 2024, RAA, 24, 025009
Matzner, C. D., & McKee, C. F. 2000, ApJ, 545, 364
McKee, C. F., & Ostriker, E. C. 2007, ARA&A, 45, 565
McKee, C. F., & Tan, J. C. 2003, ApJ, 585, 850
McMullin, J., Waters, B., Schiebel, D., et al. 2007, ASPC, 376, 127
Moharana, S., Lee, C. W., Kim, S., et al. 2026, ApJ, 997, 117
Motte, F., Bontemps, S., & Louvet, F. 2018, ARA&A, 56, 41
Padoan, P., Pan, L., Juvela, M., Haugbølle, T., & Nordlund, Å. 2020, ApJ, 900, 82
Padovani, M., Walmsley, C. M., Tafalla, M., Galli, D., & Müller, H. S. P. 2009, A&A, 505, 1199
Palau, A., Zhang, Q., Girart, J. M., et al. 2021, ApJ, 912, 159
Reid, M. J., Menten, K. M., Brunthaler, A., et al. 2019, ApJ, 885, 131
Rodríguez-Baras, M., Fuente, A., Riviére-Marichalar, P., et al. 2021, A&A, 648, A120
Sakai, N., Sakai, T., Hirota, T., & Yamamoto, S. 2010, ApJ, 722, 1633
Sanhueza, P., Jackson, J. M., Foster, J. B., et al. 2012, ApJ, 756, 60
Sanhueza, P., Liu, J., Morii, K., et al. 2025, ApJ, 980, 87
Shu, F. H., Adams, F. C., & Lizano, S. 1987, ARA&A, 25, 23
Smith, R. J., Longmore, S., & Bonnell, I. 2009, MNRAS, 400, 1775
Tan, J. C., Beltrán, M. T., Caselli, P., et al. 2014, in Protostars and Planets VI, ed. H. Beuther et al. (Univ. Arizona Press), 149
Tan, J. C., Kong, S., Butler, M. J., Caselli, P., & Fontani, F. 2013, ApJ, 779, 96
Urquhart, J. S., König, C., Giannetti, A., et al. 2018, MNRAS, 473, 1059
Urquhart, J. S., Moore, T. J. T., Csengeri, T., et al. 2014, MNRAS, 443, 1555
Valeille-Manet, M., Bontemps, S., Csengeri, T., et al. 2025, A&A, 696, A11
Vázquez-Semadeni, E., González-Samaniego, A., & Colín, P. 2017, MNRAS, 467, 1313
Vázquez-Semadeni, E., Palau, A., Ballesteros-Paredes, J., Gómez, G. C., & Zamora-Avilés, M. 2019, MNRAS, 490, 3061
Wells, M. R. A., Pillsworth, R., Beuther, H., Pudritz, R. E., & Koch, E. W. 2025, A&A, 704, A64
Xu, F., Wang, K., Liu, T., et al. 2024a, ApJS, 270, 9
Xu, F., Wang, K., Liu, T., et al. 2024b, RAA, 24, 065011
Xu, F.-W., Wang, K., Liu, T., et al. 2023, MNRAS, 520, 3259
Yamaguchi, Y., Richards, C. A., Jr., & Schaefer, H. F., III 1994, JChPh, 101, 8945
Yang, D., Liu, H.-L., Liu, T., et al. 2025a, ApJS, 280, 33
Yang, D., Liu, H.-L., Qin, S., et al. 2025b, ApJ, 995, 193
Yang, D., Liu, H.-L., Tej, A., et al. 2023, ApJ, 953, 40
Yue, Y.-H., Qin, S.-L., Liu, T., et al. 2021, RAA, 21, 014
Zhang, Q., Wang, K., Lu, X., & Jiménez-Serra, I. 2015, ApJ, 804, 141
Zhang, S., Liu, T., Wang, K., et al. 2024, MNRAS, 535, 1364
Zhang, S., Wang, K., Liu, T., et al. 2023, MNRAS, 520, 322
Zhou, J.-W., Liu, T., Evans, N. J., et al. 2022, MNRAS, 514, 6038